Green Energy and Fuel Research

Scilight

Review

Check for updates

Structural Degradation and Interfacial Failure of $LiNi_{0.8}Co_{0.1}Mn_{0.1}O_2$ Cathode: A Review of Mechanisms and Modification Strategies

Yuhui He [1,†], Haodong Xie [1,†], Yupei Han [2,†], and Weidong He [1,3,*]

[1] National Key Laboratory of Science and Technology on Advanced Composites in Special Environments, and Center for Composite Materials and Structures, Harbin Institute of Technology, Harbin 150080, China
[2] Department of Chemistry, University College London, London WC1H 0AJ, UK
[3] Chongqing Research Institute, Harbin Institute of Technology, Chongqing 401151, China
* Correspondence: weidong.he@hit.edu.cn
† These authors contributed equally to this work.
Received: 10 November 2025; Revised: 16 August 2026; Accepted: 8 September 2026; Published: 15 September 2026

Abstract: The development of sustainable energy storage systems urgently demands rechargeable lithium-ion batteries with high specific capacity and enhanced safety. Among promising cathode candidates, $LiNi_{0.8}Co_{0.1}Mn_{0.1}O_2$ (NCM811) stands out for next-generation high-energy-density applications due to its high capacity and favorable cost. However, its commercial deployment is hindered by severe structural and interfacial degradation, leading to rapid capacity fading, mechanical failure, and safety risks. This review systematically examines the fundamental degradation mechanisms of NCM811, including residual lithium-induced side reactions, transition metal dissolution, lattice oxygen release, phase transitions, microcrack propagation, and thermal runaway. Furthermore, we comprehensively summarize and critically assess representative modification strategies, including bulk doping, microstructure design, surface coating, electrolyte engineering, and the adoption of solid-state electrolytes, in terms of their effectiveness in mitigating these degradation pathways and enhancing electrochemical stability. discuss future research directions aimed at integrating multiple stabilization approaches and advancing scalable, cost-effective synthesis and processing techniques to facilitate the practical implementation of high-performance NCM811 cathodes.

Keywords: Ni-rich cathode; structural degradation; interfacial instability; modification strategies

1. Introduction

The growing need for high-energy-density storage systems, propelled by the expanding electric vehicle market and portable electronics sector, has greatly accelerated the advancement of lithium-ion batteries [1–5]. This technological push is further underscored by the global imperative to promote sustainability, particularly through the transition to renewable energy and the reduction of carbon emissions. In this context, the selection and engineering of battery materials play a pivotal role, as they directly determine the environmental footprint, resource efficiency, and lifecycle impact of energy storage systems. Among various cathode materials, particularly $LiNi_{0.8}Co_{0.1}Mn_{0.1}O_2$ (NCM811), have attracted considerable interest as promising options due to their high specific capacity and favorable operating voltage [6,7]. Nevertheless, the practical deployment of NCM811 is severely impeded by inherent chemical and structural instabilities, which result in rapid capacity fading, voltage decay, and serious safety risks, especially at high voltages [8–10].

The deterioration of NCM811 results from the intricate interaction of numerous failure mechanisms taking place at the electrode-electrolyte interface and within the bulk material [11,12]. At the interface, residual lithium compounds such as LiOH and Li_2CO_3 induce slurry gelation, elevate interfacial resistance, and initiate adverse side reactions with the electrolyte [13,14]. Concurrently, lattice oxygen release at high charge states initiates radical-driven electrolyte decomposition and gas evolution, while dissolution of transition metal (TM) further corrodes the NCM811 cathode [15]. Within the bulk material, anisotropic volume changes during lithium ion (de)intercalation accumulate microstrain and provoke microcracking, which in turn allows electrolyte to penetrate into particle interiors and accelerates the structural transformation from the initial layered configuration to spinel

Copyright: © 2026 by the authors. This is an open access article under the terms and conditions of the Creative Commons Attribution (CC BY) license (https://creativecommons.org/licenses/by/4.0/).
Publisher's Note: Scilight stays neutral with regard to jurisdictional claims in published maps and institutional affiliations.

and rock-salt phases. These interconnected processes collectively cause mechanical fracture, progressive loss of active material, and elevated electrode polarization, ultimately leading to severe performance degradation [16].

In response to these issues, the published review systematically outlines various failure mechanisms of NCM811 cathode materials, such as interfacial side reactions, bulk phase transitions, microcrack formation, and thermal runaway, while categorically elaborates on modification strategies including bulk doping, surface coating, and electrolyte optimization [17–19]. Building on this foundation, this review aims to uncover the interconnected and synergistically intensified kinetic processes among these failure modes. Furthermore, it summarizes and discusses the research progress of emerging strategies, such as high-entropy doping, locally concentrated electrolytes, functional separators, and compatibility with solid-state electrolytes. The review emphasizes the guidance of in-situ dynamic characterization and theoretical calculations in material design, while also focusing on the practical applicability and scalability potential of these strategies.

2. Intrinsic Instability and Side Reaction Mechanism

2.1. Electrode-Electrolyte Interface

2.1.1. Residual Lithium Compounds

Residual lithium compounds present on the surface is one of the fundamental sources of interfacial chemical instability in NCM811 cathode. These compounds, primarily LiOH and Li_2CO_3, are generated throughout material synthesis and post-processing [20]. During high-temperature solid-state synthesis, a stoichiometric excess of lithium source (typically 5–10% overdose) is required to compensate for lithium volatilization loss at elevated temperatures and promote crystallization of the layered structure. Upon cooling after high-temperature sintering, unstable Ni^{3+} (or Ni^{4+}) ions on the particle surface spontaneously reduce to Ni^{2+}. To maintain charge balance, lattice oxygen is oxidized and released as reactive oxygen species (e.g., O_2, O^-). These highly reactive surface oxygen species immediately react with trace H_2O and CO_2 from the ambient air, generating OH^- and CO_3^{2-} ions, which subsequently combine with the excess lithium to form surface layers of LiOH and Li_2CO_3 [21]. It is noteworthy that higher nickel content generally leads to larger specific surface area and higher surface energy. Consequently, Ni-rich materials such as NCM811 exhibit a significantly enhanced chemisorption capacity for ambient H_2O/CO_2, resulting in substantially higher residual lithium content compared to low-nickel analogues like NCM111 or NCM523 [20,22,23]. This inherent high surface alkalinity poses substantial challenges for subsequent electrode processing and electrochemical performance.

The adverse influence of surface residual lithium compounds on NCM811 cathode materials persist throughout the entire process, from electrode fabrication to battery cycling. Firstly, during electrode preparation, the strongly alkaline LiOH catalyzes the dehydrofluorination of the commonly used binder, polyvinylidene fluoride (PVDF). This leads to irreversible gelation of the slurry, significantly deteriorating its rheological properties, impairing coating uniformity, and degrading contact between active material and conductive agents. These issues directly compromise both the microstructure and macroscopic performance of the electrode [24]. Secondly, during electrochemical cycling, this insulating residual lithium layer substantially increases the charge transfer resistance (Rct), resulting in low initial coulombic efficiency and poor rate capability [25]. As shown in Figure 1a, Li_2CO_3 undergoes irreversible electrochemical oxidation at high voltages. The release of CO_2 gas in a confined battery system leads to accumulated internal pressure, causing cell swelling and posing serious safety risks [22,26].

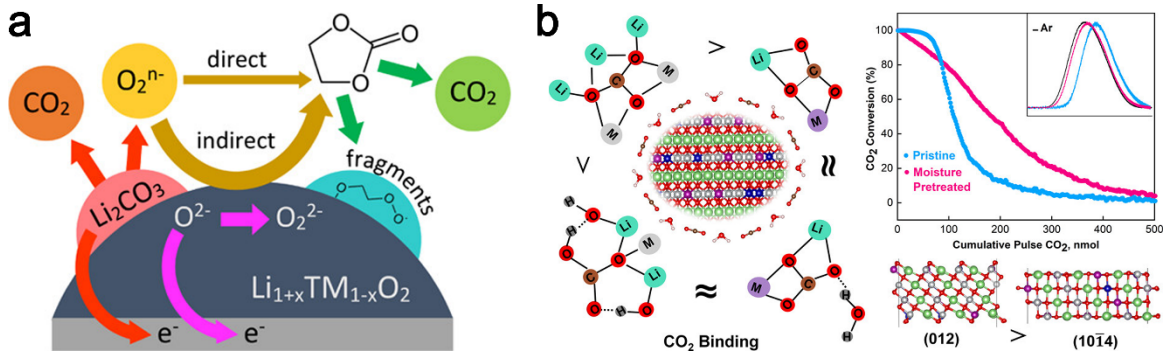


Figure 1. (**a**) The role of Li_2CO_3 in promoting electrolyte degradation through reactive oxygen species [26]. Copyright 2021, American Chemical Society. (**b**) Mechanism of surface impurity formation on NCM811 upon exposure to CO_2 and H_2O [27]. Copyright 2021, American Chemical Society.

More critically, surface lithium compounds trigger electrolyte decomposition. $LiPF_6$ hydrolysis generates the Lewis acid PF_5, which further reacts with trace water to produce highly corrosive HF. HF then reacts with Li_2CO_3. This process not only continuously consumes the electrolyte and thickens the interface layer but also regenerates water molecules that further promote $LiPF_6$ hydrolysis (Figure 1b). This establishes an autocatalytic degradation cycle, persistently corroding the cathode surface and accelerating transition metal dissolution [27].

2.1.2. Lattice Oxygen Release and Interfacial Catalytic Decomposition

Lattice oxygen release and the ensuing interfacial catalytic decomposition reactions constitute a fundamental cause of the rapid capacity fade and safety concerns in NCM811 cathodes operated at high voltages [28,29]. This process is driven by electronic structure instability under deep delithiation [30]. When the charging voltage exceeds 4.3 V (vs. Li^+/Li), Ni ions are extensively oxidized to Ni^{4+}, which exhibits a strong tendency to gain electrons. The resulting energy band overlap between Ni 3d (t_{2g}) and O 2p orbitals prompts a charge transfer from oxygen anions to nickel cations. This shifts the O 2p band center upward, leading to the oxidation of some oxygen atoms and the formation of peroxide-like species (O^{2n-}, n = 1 or 2) or highly reactive singlet oxygen ($^1O_2$), ultimately evolving as gaseous oxygen from the lattice [31,32].

The release of lattice oxygen initiates a catastrophic chain reaction. Firstly, the formation of oxygen vacancies directly disrupts the crystal framework, serving as nucleation sites for detrimental bulk phase transformations. More critically, the released reactive oxygen species (e.g., $^1O_2$) efficiently attack the nucleophilic carbonyl oxygen in ethylene carbonate (EC) molecules, triggering a series of free radical reactions that ultimately generate byproducts such as CO_2, CO, H_2O, and polycarbonates [33]. This process not only irreversibly consumes the electrolyte, but the generated gases (particularly CO_2) can cause cell swelling, posing serious safety risks. Furthermore, the newly formed water molecules react with $LiPF_6$ to produce more HF, which in turn exacerbates cathode corrosion and transition metal dissolution, establishing a vicious side-reaction cycle [34,35].

The electrolyte decomposition reactions triggered by lattice oxygen release build a loose, thick, and highly resistive cathode-electrolyte interphase (CEI) on the cathode surface. This inferior CEI fails to effectively suppress subsequent oxygen release and electrolyte decomposition. Its continual, dynamic growth persistently consumes active lithium ions, leading to drastically increased polarization and capacity fading [34]. As shown in Figure 2, it is important to note that lattice oxygen loss and interfacial side reactions are not isolated events. They are intrinsically linked to the bulk structural degradation of the material [18]. On one hand, the generation of oxygen vacancies lowers the migration energy barrier for transition metal ions (especially Ni), promoting an irreversible structural reconstruction from the layered phase (R-3m) to spinel (Fd-3m) and finally to a rock-salt phase. On the other hand, the microstrain induced by the abrupt *c*-axis contraction during the H2–H3 phase transition is believed to further aggravate oxygen loss in the near-surface region. This chemo-mechanical coupling failure mechanism keeps the NCM811 interface in a state of continuous and dynamic degradation under high-voltage operation. Consequently, suppressing lattice oxygen release is regarded as pivotal for enhancing the high-voltage stability of NCM811 [35].

2.1.3. Transition-Metal Dissolution and Cross-Talk with the Anode

TM dissolution constitutes another severe consequence of interfacial chemical instability in NCM811 cathodes, a process governed by both chemical and electrochemical pathways. Chemically, hydrofluoric acid generated from $LiPF_6$ hydrolysis directly attacks the cathode surface, reacting with TM-O bonds and leading to the dissolution of TM ions, primarily in their divalent states [36,37]. As shown in Figure 3a, the dissolution of manganese occurs predominantly through the disproportionation reaction of Mn^{3+}, which explains why the dissolved proportion of Mn often exceeds its stoichiometric ratio in NCM materials [38]. Electrochemically, unstable Ni^{4+} and Co^{4+} species at high operating voltages tend to undergo direct reduction and dissolution, a process frequently accompanied by lattice oxygen release [39]. Notably, microcracks resulting from anisotropic volume changes and H2–H3 phase transitions drastically increase the active material-electrolyte contact area (Figure 3b) [40]. These microcracks provide efficient pathways for HF penetration and TM dissolution, thereby dramatically accelerating material degradation.

TM ions migrate through the electrolyte and separator, ultimately reaching the anode surface. These ions are then reduced and deposited within the solid electrolyte interphase (SEI) [41]. Functioning as highly efficient catalysts, these metallic deposits promote continuous electrolyte reduction at the anode interface. This catalytic activity drives uncontrolled SEI thickening, progressively consuming both lithium ions and electrolyte components. More critically, these TM ions inclusions compromise SEI homogeneity, promoting lithium dendrite growth and creating substantial internal short-circuit risks [42].

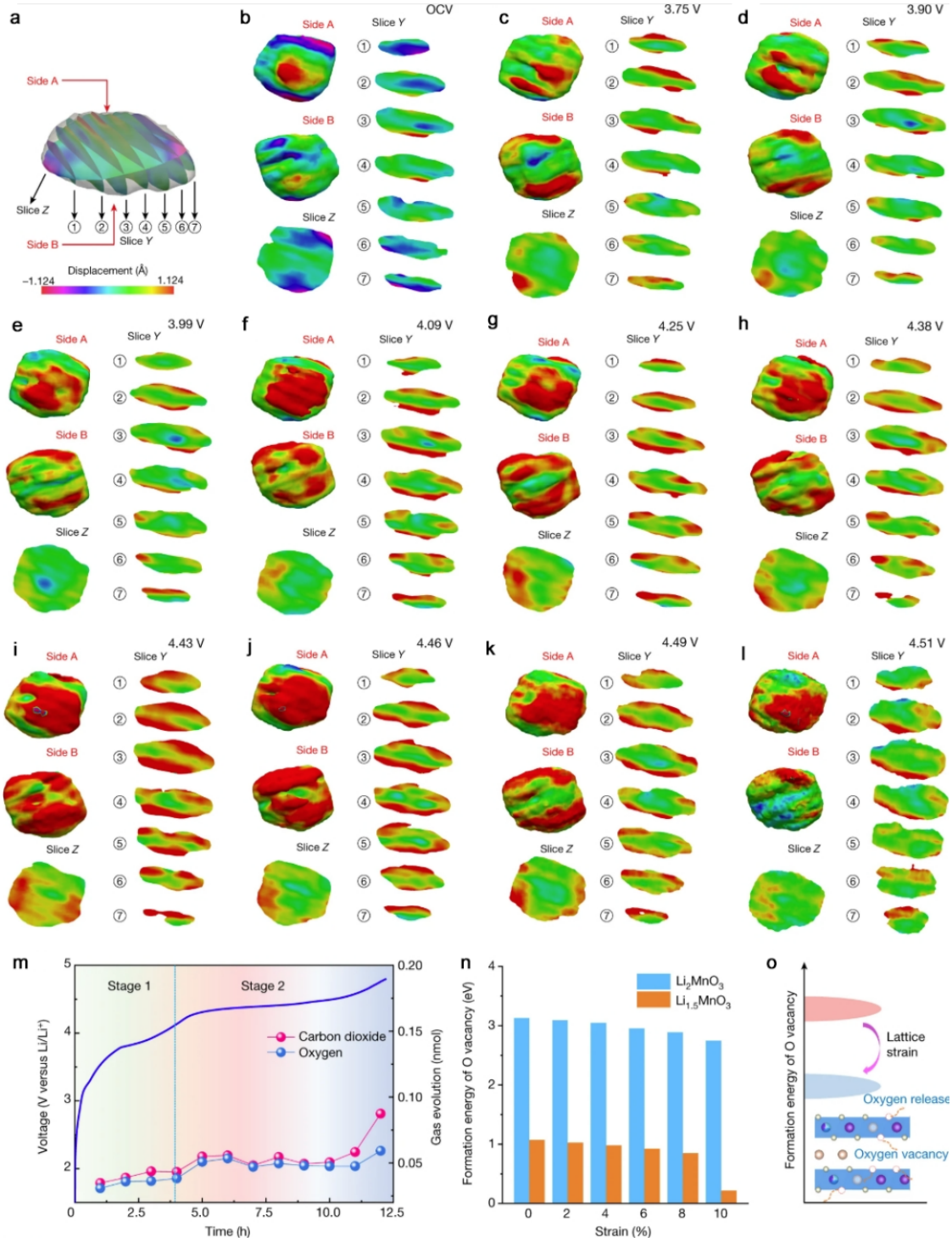


Figure 2. (**a**–**l**) In situ (**a**) BCDI images of the 3D LMR particle in the strain field, measured at 3.2 V (OCV) (**b**), 3.75 V (**c**), 3.90 V (**d**), 3.99 V (**e**), 4.09 V (**f**), 4.25 V (**g**), 4.38 V (**h**), 4.43 V (**i**), 4.46 V (**j**), 4.49 V (**k**) and 4.51 V (**l**). The compressive and tensile strains are expressed by blue and red colors, respectively. The strain evolution in each state is detailed by the spatial location of the slices along the y axis. (**m**) In situ differential electrochemical mass spectroscopy measurements for the LMR primary particle. (**n**) Formation energy of O vacancies in Li_2MnO_3 and $Li_{1.5}MnO_3$ when tensile strains are applied. (**o**) Schematic illustration of the influence of lattice strain on O release [18]. Copyright 2022, Springer Nature. The lattice strain at high voltage promotes oxygen loss, accelerating structural degradation.

TM dissolution exhibits intricate interconnections with other degradation pathways. As previously established, microcracking accelerates TM dissolution. Meanwhile, the continuous CEI/SEI growth and lithium depletion resulting from TM dissolution promote lattice oxygen evolution via elevated polarization and localized overcharging. Furthermore, the stoichiometric imbalance created by TM leaching from the cathode surface

establishes thermodynamically favorable conditions for cation mixing and subsequent reconstruction of rock-salt surface phases [36,43]. Consequently, TM dissolution serves as a critical nexus linking cathode and anode degradation mechanisms, ultimately accelerating performance decay in full-cell configurations.

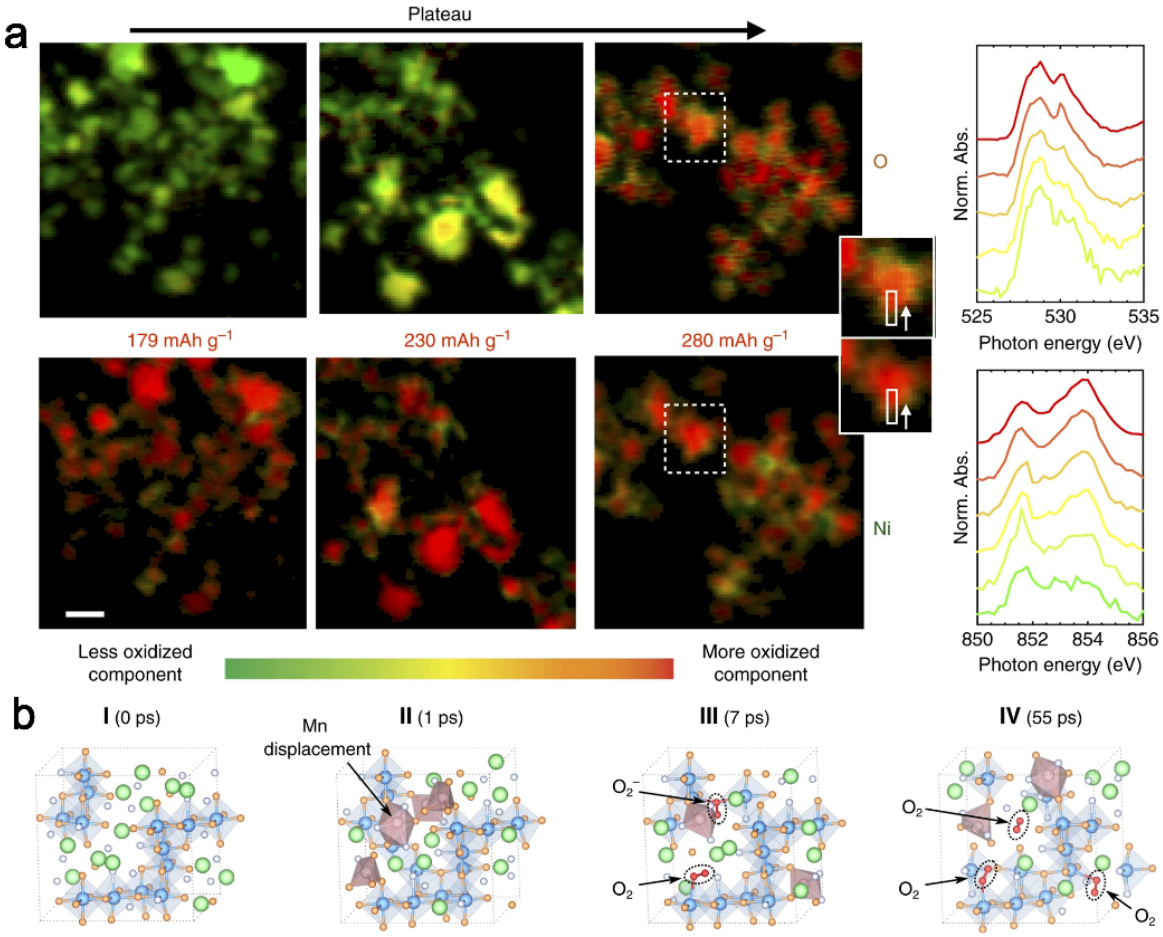


Figure 3. (**a**) Left: nanoscale spatial distribution of end-member phases within a primary particle at different points during the voltage plateau. Right: by amplifying the spectral line scanning of the particles, the oxidation of bulk oxygen along the surface of nickel and the reduction of oxygen are revealed. Spectra at the top and bottom correspond to the bulk and near-surface regions, respectively [38]. Copyright 2017, Springer Nature. This figure demonstrates the strong coupling between transition metal dissolution and oxygen redox activity, particularly at the particle surface. (**b**) Geometry of relaxed crystal structures, highlighting events of manganese migration and O-O dimerization. Pink polyhedra indicate Mn ions displaced from the original octahedral position in the rocksalt structure [40]. Copyright 2022, Springer Nature.

2.2. Degradation of Body Structure and Mechanical Integrity

2.2.1. Detrimental Phase Transition

The structural degradation of NCM811 during prolonged cycling and high-voltage operation conditions involves a series of irreversible detrimental phase transformations. This process typically initiates with surface cationic disordering [44]. Given the comparable ionic radii of Ni^{2+} (0.69 Å) and Li^{+} (0.76 Å), a fraction of Ni^{2+} ions spontaneously migrates to octahedral sites within the lithium layer during material synthesis or electrochemical cycling, particularly under conditions of abundant lithium vacancies during charging [45,46]. This Li/Ni antisite exchange not only blocks two-dimensional diffusion pathways for lithium ions, thereby impairing rate capability, but also serves as the initial stage of structural collapse [47,48].

During prolonged cycling, especially under high-voltage operation, the Ni^{2+} that has migrated into the lithium layers trigger local lattice rearrangement to reduce the system energy [49,50]. As shown in Figure 4a, this process drives an irreversible transition from the initial layered (R 3m) to a spinel (Fd 3m) structure [51]. The spinel structure exhibits sluggish ion kinetics, resulting in voltage plateau decay and increased polarization.

Ultimately, continuous TM migration, accompanied by lattice oxygen release, leads to the complete conversion of the surface region into a disordered rock-salt phase (Fm-3m) structurally analogous to NiO (Figure 4b,c) [52,53]. This rock-salt phase lacks continuous pathways for lithium-ion migration, completely blocking lithium deintercalation and leading to irreversible capacity loss [54].

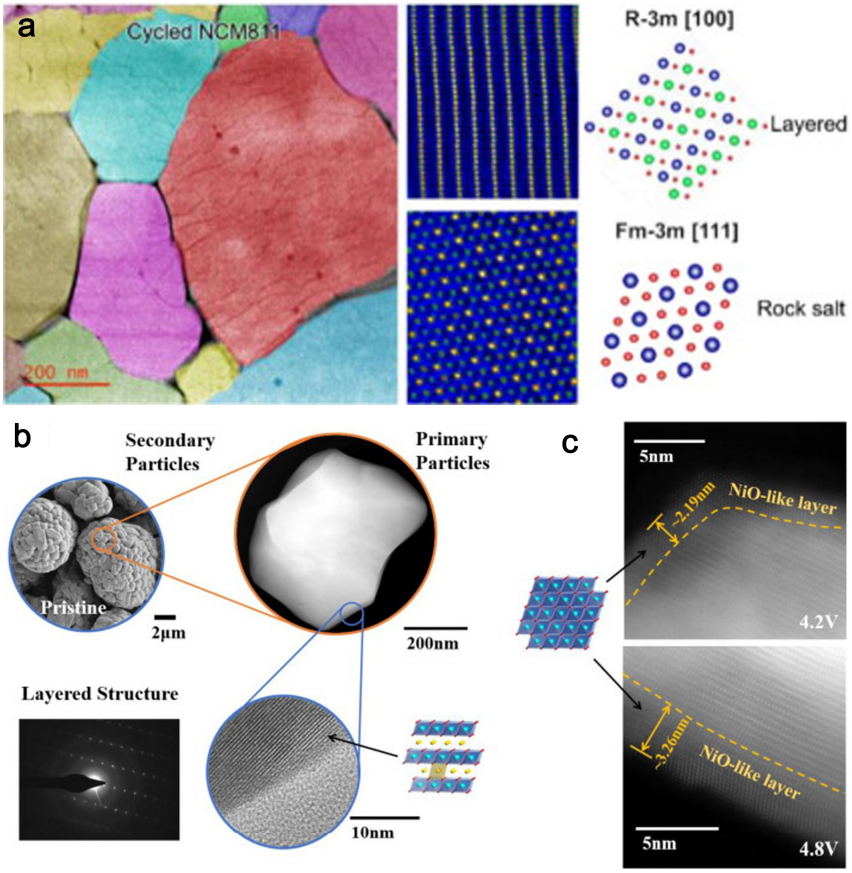


Figure 4. (**a**) Structural evolution of an NCM811 cathode, showing the direct transformation accompanied by severe intergranular cracking [51]. Copyright 2022, Science Press and Dalian Institute of Chemical Physics, Chinese Academy of Sciences. (**b**) TEM images and corresponding selected-area electron diffraction (SAED) images of a pristine NCM811 particle, indexed to the layered R-3m structure. (**c**) High-resolution TEM images of NCM811 samples [53]. Copyright 2021, Science Press and Dalian Institute of Chemical Physics, Chinese Academy of Sciences.

This phase transformation initiates at the surface of the particles and gradually expands into the bulk material with cycling, forming a core-shell structure, which constitutes a fundamental origin of impedance growth and irreversible capacity fade [55]. Notably, the H2 to H3 phase transition occurring around 4.2 V, accompanied by a rapid contraction along the *c*-axis, represents a primary driver for the development of microstrain and microcracks within NCM811 particles [18,47].

2.2.2. Anisotropic Volume Changes

The pronounced anisotropic volume changes exhibited by NCM811 during charge and discharge cycles constitute the physical origin of its mechanical integrity failure. This anisotropic behavior originates from the intrinsic characteristics of its layered crystal structure [56].

During lithium extraction, the oxidation of nickel and consequent shortening of TM-O bonds induce progressive contraction along the *a*-axis, which reflects in-plane TM-O bond lengths [57]. Simultaneously, the *c*-axis, which reflects the spacing between adjacent oxygen layers, initially expands due to enhanced interlayer oxygen-oxygen electrostatic repulsion following lithium removal. However, upon charging into high-voltage regions, it undergoes an abrupt contraction [58,59]. This contraction is fundamentally linked to electronic structure evolution at high degrees of delithiation. When the lithium content x(Li) falls below 0.5, extensive oxidation of Ni to Ni^{4+} enhances Ni-O orbital hybridization, increasing covalent character in Ni-O bonds. This enhanced covalency weakens interlayer electrostatic repulsion, causing contraction within the TM oxide slabs and ultimately driving

the collapse of the *c*-axis [60,61]. As shown in Figure 5a,b, the highly anisotropic lattice strain resulting from continuous *a*-axis contraction and the initial expansion followed by sudden contraction of the *c*-axis generates substantial internal stress within secondary particles [62]. Accumulation of this stress directly provides the driving force for microcrack initiation. When local stress exceeds the grain boundary cohesive strength, cracks preferentially nucleate and propagate along primary particle boundaries. Notably, anisotropic volume change is tightly coupled with detrimental phase transformations. the H2–H3 phase transition directly induces the abrupt *c*-axis collapse, while the transition itself is driven by cationic mixing [63]. Consequently, stress accumulation essentially represents the mechanical manifestation of a cascade of changes spanning electronic structure, crystal lattice, and particle microstructure during electrochemical cycling [64]. Studies further indicate that the magnitude of this lattice strain not only correlates positively with nickel content, but is also exacerbated by external factors such as rate and electrode thickness [65]. These factors promote heterogeneous lithium-ion concentration distributions, leading to coexisting phase domains and localized stress mismatch, which further accelerates microcrack formation and particle fracture.

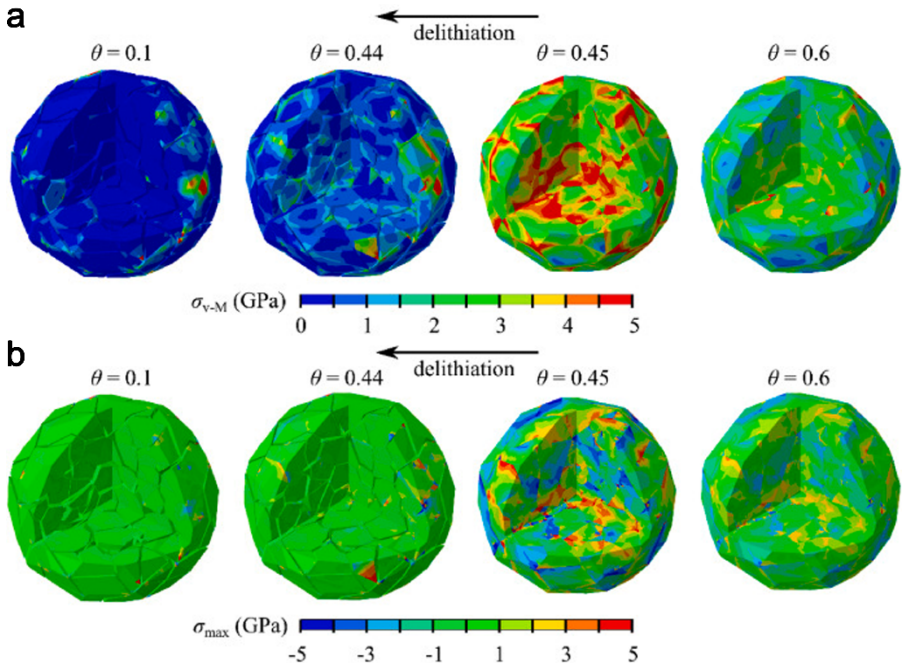


Figure 5. (**a**) Predictions of the evolution of von-Mises stress (**a**) and principal stress σ_{max} (**b**) within the secondary particle upon delithiation from $\theta = 1$ for the choice $G_{wf} = 2$ Jm^{-2} [62]. Copyright 2023, Elsevier B.V. The simulation reveals that anisotropic volume changes generate significant internal stress, which is the primary driver for microcrack initiation.

2.2.3. Initiation and Propagation of Microcrack

Microcracks in NCM811 are primarily categorized into intergranular and intragranular cracks. As discussed in the preceding section, intergranular cracks originate from stress accumulation at secondary particle grain boundaries caused by anisotropic volume changes. They represent the dominant crack mode during the initial and middle stages of cycling [66]. As shown in Figure 6a–h, intragranular cracks initiate within primary particles, typically associated with crystalline defects and localized stress concentration, becoming prevalent under higher voltages (>4.5 V) and prolonged cycling [67]. Intragranular crack development is governed by several nanoscale mechanisms. Firstly, lithium deintercalation can be inhomogeneous even within a single crystallite, creating nanoscale gradients in lattice parameters and generating internal stress [68]. Secondly, in regions with high dislocation density, dislocations can migrate, pile up, and act as nucleation sites for cracks under cyclic stress. Furthermore, the migration and coalescence of oxygen vacancies generated by lattice oxygen release can form nanovoids (Figure 6i,j) [69]. This process compromises the local structural integrity, thereby directly initiating intragranular cracking [70,71]. Intragranular cracks compromise the structural coherence of particles, impede intra-granular lithium-ion diffusion, and increase polarization. More critically, they provide pathways for electrolyte penetration into particle interiors, severely exacerbating interfacial side reactions, TM dissolution, and rock-salt phase reconstruction. This, in turn, intensifies local strain and stress concentration, ultimately leading to the complete pulverization of secondary particles [16,72].

Collectively, intergranular and intragranular cracks constitute a comprehensive mechanical degradation scheme. Intergranular cracks compromise the macroscopic integrity of secondary particles, while intragranular cracks degrade ionic transport within primary particles at the microscopic scale and facilitate electrolyte ingress, triggering severe interfacial side reactions [38,41]. These reactions and their accompanying phase transformations generate additional strain, which further promotes the initiation and propagation of more cracks. This "cracking-infiltration-side reactions-further cracking" vicious cycle constitutes the core mechanism ofaccelerated capacity decay and structural pulverization of NCM811.

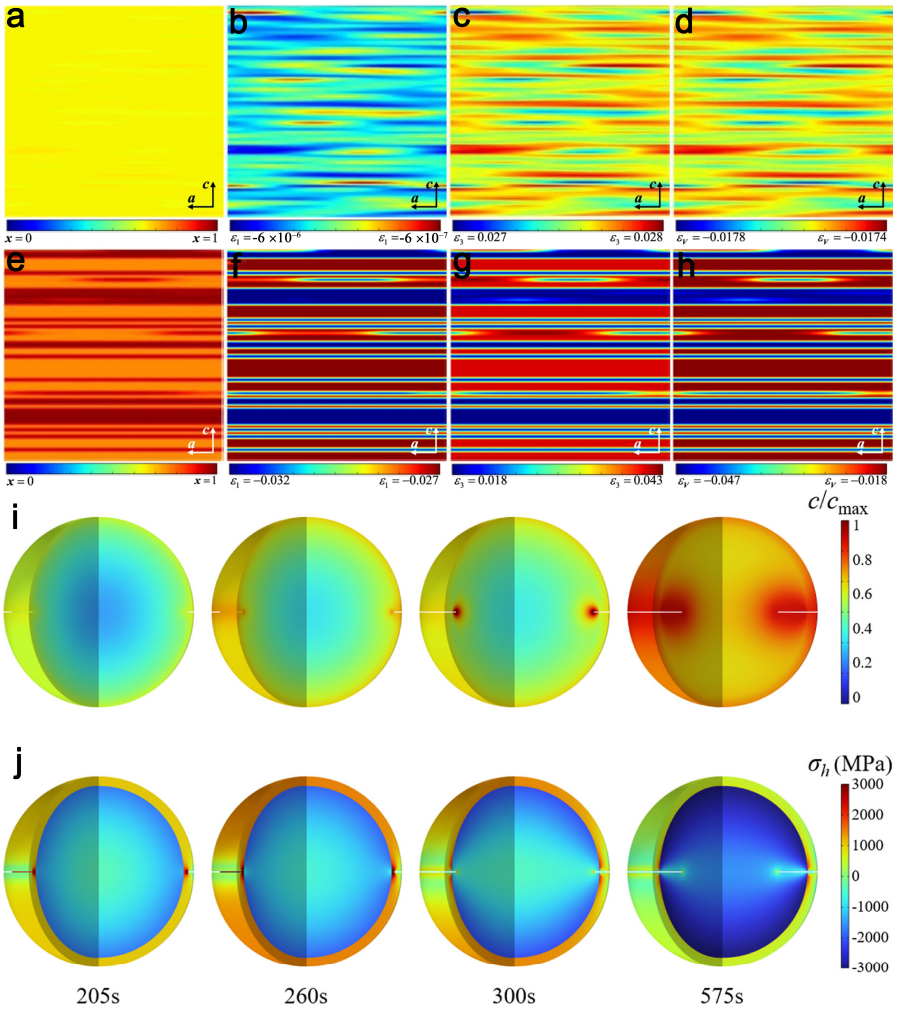


Figure 6. (**a**–**h**) Meso-scale phase transformations in the nanodomain with dimensions of 31.36 × 31.36 nm in $Li_{1-x}Ni_{0.8}Co_{0.1}Mn_{0.1}O_2$ at room temperature (300 K) from a solid solution of inverse Li concentration x = 0.65 (**a**–**d**) and 0.85 (**e**–**h**) at dimensionless time = 5, (**a**,**e**), (**b**,**f**), (**c**,**g**), and (**d**,**h**) are the distributions on the ac plane of the inverse Li concentration x, strain in a direction ε1, strain in c direction ε3, and volumetric strain εV, respectively [67]. Copyright 2017, Springer Nature. (**i**,**j**) Propagation of cracking in a spherical core-shell NCM electrode particle during lithiation at a 5C rate: (**i**) spatial and temporal distribution of normalized Li concentration, and (**j**) corresponding distribution of hydrostatic stress [69]. Copyright 2024, American Chemical Society. These models show that inhomogeneous lithium (de)intercalation leads to localized strain and stress concentrations, which initiate intragranular cracks.

2.3. Thermal Instability

While delivering high-energy-density, NCM811 poses substantial safety concerns due to its intrinsic thermal instability [73]. Thermal runaway, which is an uncontrollable self-heating process driven by exothermic chain reactions, primarily stems from the intense heat release associated with high temperature decomposition of NCM811 and its interactions with the electrolyte. This process is typically triggered by overcharging, mechanical penetration, or external heating [74].

The thermal instability of NCM811 manifests in several critical aspects. As shown in Figure 7a, firstly, the material exhibits significantly compromised thermal stability at high states of charge [75]. As temperature rises,

unstable Ni^{4+} ions trigger rapid lattice oxygen release. The evolved reactive oxygen species violently attack the electrolyte, producing large amounts of heat and gas, leading to a sharp rise in internal pressure and temperature [76,77]. Additionally, oxygen evolved from the cathode reacts vigorously with electrolyte components, releasing significant volumes of CO_2 and CO along with intense heat [78,79]. Moreover, the inferior CEI decomposes at elevated temperatures, exposing fresh, highly active surfaces that further accelerate parasitic reactions. The cumulative effects of microcracking and interfacial side reactions create additional active surfaces and defects, supplying more heat sources for thermal runaway [80–82]. These gradually evolving degradation mechanisms become drastically accelerated and amplified under thermal abuse conditions. Through a tightly interwoven series of exothermic reactions, they ultimately drive the cell into an irreversible state of thermal runaway (Figure 7b) [83].

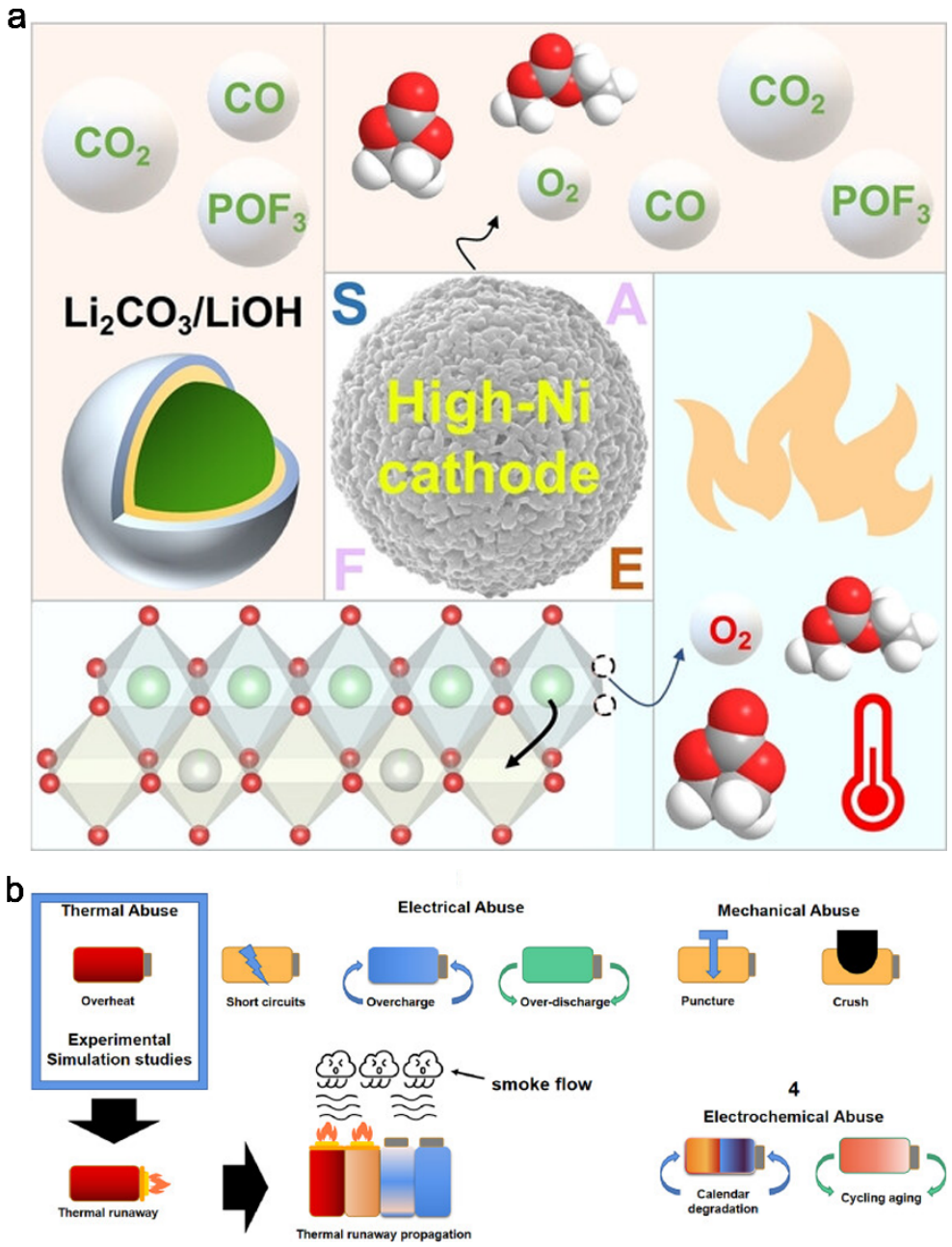


Figure 7. (**a**) Proposed mechanism for the thermal decomposition of Ni-rich cathode [75]. Copyright 2023, Wiley-VCH. (**b**) Factors initiating thermal runaway of a single battery and those enabling its propagation within multi-cell modules [83]. Copyright 2024, Elsevier B.V.

3. Collaborative Inhibition Strategy

3.1. Bulk Doping

Bulk doping is an atomic-scale strategy aimed at enhancing the intrinsic stability of materials. By introducing foreign elements, it modulates the local electronic structure and bonding characteristics of the TM layer, thereby

suppressing the structural degradation of high-nickel materials [84]. Depending on the charge and site occupancy of the dopants, the stabilization mechanisms primarily include suppressing cation disorder, mitigating anisotropic lattice strain, and strengthening the TM-O bonds to inhibit oxygen loss [85].

3.1.1. Cationic Doping

Cationic doping represents the most extensively studied doping strategy, exhibiting the greatest diversity in mechanistic effects. As shown in Figure 8a, Sun et al. incorporated Ta into a Ni-rich cathode [86]. The segregation of Ta at grain boundaries and particle surfaces suppresses the migration and diffusion of Ni ions, thereby effectively maintaining the microstructural stability. Concurrently, this segregation provides an inert layer that inhibits electrolyte side reactions and prevents surface degradation. As depicted in Figure 8b, Aurbach et al. employed an approach involving the coating of cathode material particles with a precursor containing the dopant, followed by high temperature annealing to facilitate dopant diffusion into the particle bulk [87]. This "top-down" method enabled rapid screening of dopant effects for Mg^{2+}, Al^{3+}, Si^{4+}, Ti^{4+}, Zr^{4+}, and Ta^{5+}. High-valence cations with large ionic radii (e.g., Zr^{4+}, Ti^{4+}, Ta^{5+}) preferentially occupy TM sites, inducing a significant "pillar effect" owing to their high charge and large ionic radius. The exceptional stability of ions like Zr^{4+} and Ta^{5+} in TM sites, resisting migration, combined with their high charge exerting strong electrostatic repulsion on surrounding ions, significantly increases the energy barrier for Ni^{2+} migration from the TM layer to the Li layer. This effectively suppresses cation disordering. Some high-valence ions, such as W^{6+}, form exceptionally strong W-O covalent bonds with lattice oxygen due to their extreme oxidation state. This markedly increases the formation energy of oxygen vacancies, making lattice oxygen less susceptible to release under high voltage. This mechanism not only enhances the thermal stability of the material but also blocks detrimental phase transitions induced by oxygen loss. Zhou et al. developed a simple method for W/Nb co-doping of NCM811 [88]. The co-doped cathode maintained capacity retentions of 54.9% after 400 cycles. As illustrated in Figure 8c, Ou et al. established an *in situ* doping strategy that enhances the homogeneity of cation doping [89]. The uniform incorporation of Nb^{5+} effectively suppressed intragranular crack formation and interfacial degradation.

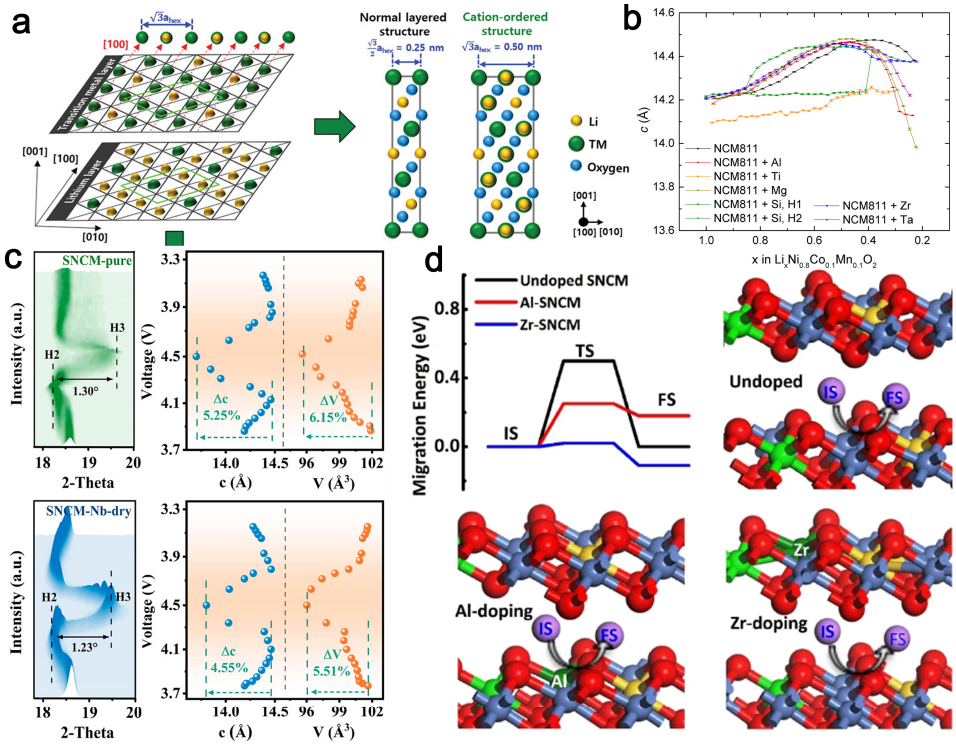


Figure 8. (**a**) Schematic diagrams comparing the atomic arrangements of a standard layered and cation-ordered structure [86]. Copyright 2023, Wiley-VCH. (**b**) *c*-lattice parameters as a function of the lithium content x in $Li_xNi_{0.8}Co_{0.1}Mn_{0.1}O_2$ calculated from in situ XRD measurements of NCM811 electrodes [87]. Copyright 2019, American Chemical Society. (**c**) In situ XRD patterns and the corresponding lattice parameter changes of the prepared cathodes during the initial cycle between 2.5 and 4.5 V [89]. Copyright © 2024, American Chemical Society. (**d**) Migration energy and corresponding schematic structure for undoped cathodes, Al or Zr doped cathodes (Al-SNCM and Zr-SNCM): IS, TS and FS represent initial state, transition state, and final state, respectively [90]. Copyright 2022, Springer Nature.

Dopants with ionic radii similar to Li^+ can enlarge the interlayer spacing and reduce cation disorder, thereby promoting Li^+ transport and inhibiting severe lattice contraction during high-voltage charging. This alleviates structural stress and crack formation, ultimately leading to more stable electrochemical performance. Lu et al. developed an Al/Zr co-doped single-crystal $LiNi_{0.88}Co_{0.09}Mn_{0.03}O_2$ (SNCM) cathode material (Figure 8d) [90]. The highly soluble Al^{3+} ions were fully incorporated into the lattice, enhancing Li^+ mobility, relieving internal strain, and suppressing cation disordering during cycling to high cutoff voltages. The less soluble Zr^{4+} ions contributed to forming a stable CEI, inhibiting electrolyte side reactions. Sun et al. proposed a dual-doping strategy using Al^{3+} and Nb^{5+} ions to improve the cycling stability of Ni-rich cathodes [91]. The Al^{3+} ions suppressed cation mixing, while the Nb^{5+} ions promoted the transformation of cathode particles into a radially aligned rod-like morphology. Huang et al. utilized Na^+ as a co-dopant to facilitate the introduction and supersaturated enrichment of Ti^{4+} in the near-surface region of NCM811 (NT-NCM), forming a modified layer approximately 9 nm thick [92]. This co-doping strategy induced a unique surface structure at the cathode surface and grain boundaries, characterized by partial ordering, cation densification, and expanded lattice spacing. This structure, distinct from a fully disordered rock-salt phase, remains electrochemically active while exhibiting enhanced robustness.

Cationic doping has been widely demonstrated as an effective strategy for enhancing the cycling stability of NCM811. Current research is evolving from single-element doping towards the development of co-doping strategies, which requires rational design of dopant combinations, concentrations, and spatial distributions [59,93]. Further investigation is needed to elucidate the valence evolution and synergistic mechanisms of multiple dopant ions during both the synthesis and electrochemical cycling of NCM811 cathodes.

3.1.2. Anionic Doping

Anionic doping involves the partial substitution of O^{2-} in the lattice with F^-, Cl^-, or polyanions (e.g., PO_4^{3-}, BO_3^{3-}), enabling regulation at the anionic sublattice level. F^- doping is the most widely studied anionic doping strategy [94,95].

Yu et al. developed a strategy for fluorinated Ni-rich cathodes by introducing D atoms into the oxygen layers to create a F-rich interface (Figure 9a) [96]. Due to the high electronegativity of F, the partial substitution of O^{2-} by F^- significantly enhances the ionic character of the TM-anion bond, forming more stable TM-F bonds. This change considerably increases the formation energy for oxygen vacancies, thereby effectively suppressing the release of lattice oxygen. Moreover, the fluorinated interface serves as a barrier against interfacial side reactions and encourages the development of a stable CEI. As illustrated in Figure 9b, Wu et al. utilized F-doping to deliberately induce beneficial cation antisite defects [97]. This strategy significantly improved the cycling and thermal stability of the Ni-rich layered cathodes. When F substitutes lattice oxygen, the much stronger F-Li bond compared to the F–Ni bond promotes local Li–Ni cation exchange, forming a more stable local halide octahedral structure with lower energy, thereby enhancing lattice stability. Yu et al. prepared a P-doped cathode via an in situ gas-solid interfacial phosphorylation reaction (Figure 9c) [98]. The stable CEI suppresses electrolyte side reactions and facilitates Li^+ transport. The P-O bonds effectively stabilize lattice oxygen, enhancing the cycling stability.

As depicted in Figure 9d, Liu et al. fabricated a borate polyanion-doped Ni-rich cathode using gradient engineering and a surface disordered phase strategy [95]. B doping induces Ni^{2+} migration to the Li layers, forming a ~2 nm thick ordered-disordered layered coherent structure on the surface that enhances mechanical and chemical stability. The strong covalent B-O tetrahedral configuration strengthens lattice oxygen stability and inhibits oxygen release.

Anionic doping enhances NCM811 stability through reinforced TM-anion bonds, stabilizing lattice oxygen, and optimizing interfacial structures [99,100]. Further investigation is needed to understand the site occupation mechanisms of anionic doping and to develop synergistic strategies involving different anions.

3.1.3. Multi-Ion Co-Doping

Cationic-anionic co-doping aims to achieve more comprehensive and precise regulation of NCM811 cathode through the complementary and synergistic effects of different dopants, thereby overcoming the performance limitations of single-element doping. Dai et al. implemented a triply coupled modification via $NaPF_6$ hydrolysis [101]. This approach incorporated Na^+ and F^- into the Ni-rich cathode material in a concentration gradient, significantly suppressing cation disorder. Furthermore, the constructed NaF coating facilitated the in situ formation of a thin, dense, LiF-rich CEI layer on the cathode surface. As shown in Figure 10a, Guo et al. co-doped PO_4^{3-} polyanions and Mn^{4+} cations into the cathode by a high-temperature solid-state method [102]. The introduction of Mn^{4+} stabilized the TM layer structure and reduced Ni^{2+} formation, thereby significantly decreasing Li/Ni mixing. The incorporation of large-volume PO_4^{3-} polyanions into the lattice substantially expanded the lithium layer spacing, enhancing Li^+ migration rates. Moreover, the PO_4^{3-} and Mn^{4+} co-doping stabilized the crystal structure and

increased the energy barrier for phase transitions, leading to significant suppression of the H2–H3 phase transition. Hu et al. utilized Na^+ and Br^- co-doping to enhance both the structural stability and lithium-ion transport kinetics of a Ni-rich cathode [103]. Na^+ expanded the Li layer spacing and alleviated Li/Ni cation mixing. Meanwhile, the partial substitution of O^{2-} by Br^-, to maintain charge balance, caused the reduction of some Ni^{3+} to Ni^{2+}. The decreased population of Jahn-Teller active ions (Ni^{3+}) inhibited lattice distortion and enhanced structural stability. The resulting Ni^{2+} ions preferentially migrated to the lithium layers, creating Li/Ni antisite defects at the surface that effectively resisted *c*-axis contraction under high voltage, thereby suppressing microcrack formation.

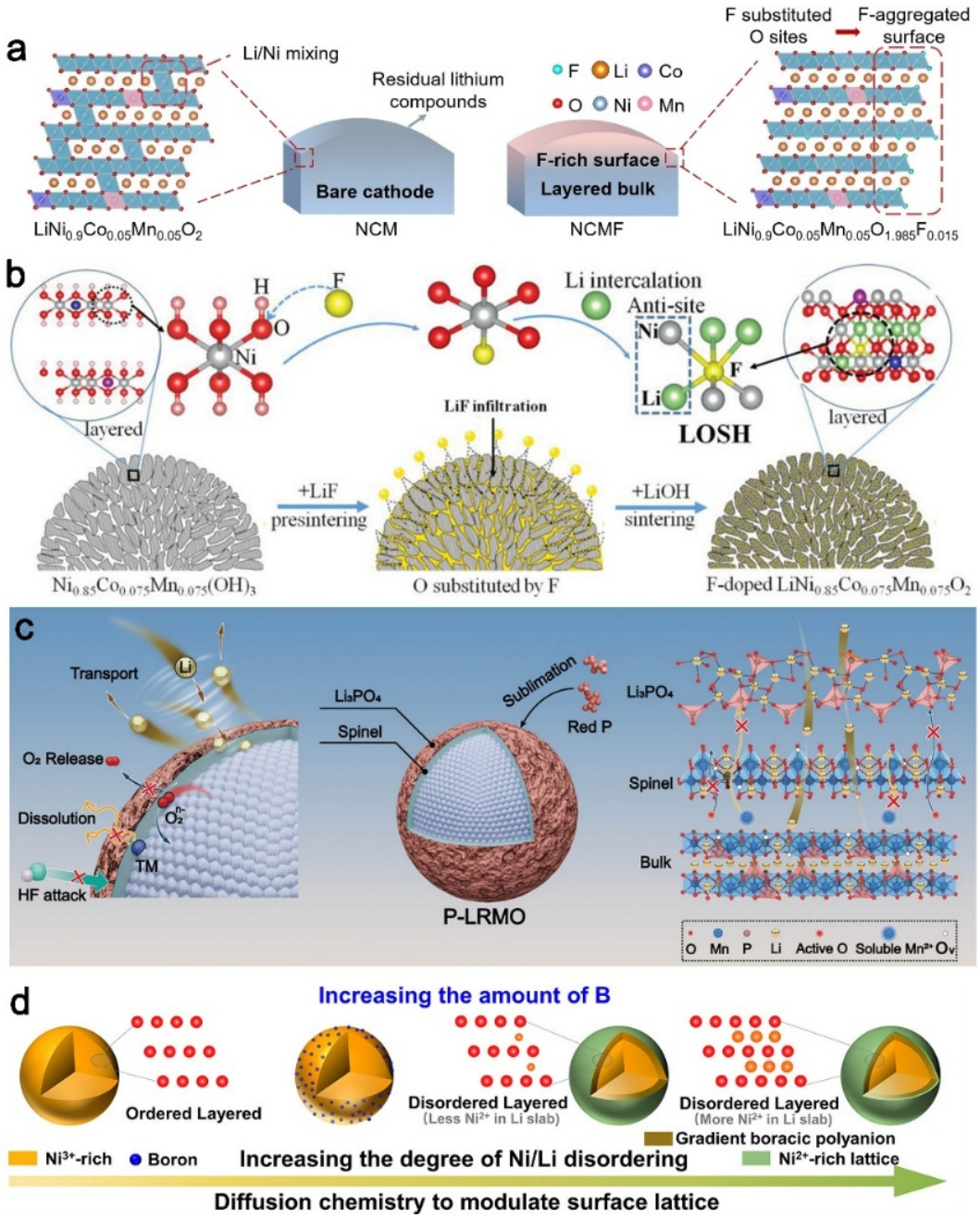


Figure 9. (**a**) The crystal structures of NCM and fluorinated NCM (NCMF) were compared [96]. Copyright 2024, Wiley-VCH. (**b**) Schematic of the preparation process for AS-LNCM, illustrating the migration of LiF compounds into $Ni_{0.85}Co_{0.075}Mn_{0.075}(OH)_3$ precursor particles and subsequent reaction leading to partial oxygen substitution by fluorine [98]. Copyright 2018, John Wiley and Sons. (**c**) Schematic diagram of the phosphatizing surface modification process [97]. Copyright 2024, Wiley-VCH. (**d**) Schematic diagram of the surface phase structure evolution of NCM induced by varying boron (B) content [95]. Copyright 2023, American Chemical Society.

The high-entropy stabilization strategy, a significant breakthrough in materials science, has recently demonstrated considerable potential in Ni-rich cathodes. Xin et al. introduced four low-concentration dopant elements into a Ni-rich cathode while preserving its host structure, creating a local high-entropy environment

within the TM sublattice (Figure 10b,c) [104]. This heterogeneous chemical environment effectively suppressed abrupt lattice changes and volume variations during charge/discharge, thereby preventing microcrack initiation. The multiple high-valence dopants disrupted the chain reaction of oxygen vacancy migration, aggregation, and subsequent oxygen release, substantially enhancing the thermal stability and structural integrity. Zhang et al. proposed Ta^{5+}/Br^{-} co-doping as a strategy to modulate the electronic band center, thereby suppressing lattice oxygen release and detrimental phase transitions in high-nickel cathodes under high-voltage operation [105]. The strong Ta-O bonds, synergistically coupled with the low-electronegativity Br^{-} anions, reduce electrostatic repulsion in the O-TM-O framework. This adjustment shifts the band centers of Ni 3d and O 2p orbitals and widens the bandgap, effectively inhibiting oxygen escape driven by Co 3d-O 2p hybridization. Furthermore, the doping expands the lattice spacing, alleviating volumetric strain during Li^{+} (de)intercalation and significantly delaying the H2–H3 phase transition along with its associated lattice distortion. As a result of the suppressed oxygen release and phase changes, side reactions between the cathode and electrolyte are mitigated. This leads to the formation of a thinner and more stable CEI after cycling, accompanied by a marked reduction in intraparticle cracking.

In summary, cationic-anionic co-doping enables synergistic optimization of the interfacial properties, crystal and electronic structure of NCM811. Future efforts should leverage theoretical computations and machine learning to design optimal cationic-anionic combinations and their spatial distributions (e.g., gradient doping) for maximizing synergistic effects. The development of novel synthesis methods capable of achieving atomic-level precision in dopant placement, including precise control over spatial distribution such as concentration gradients, is crucial to construct a comprehensively stabilized structure from the bulk to the interface.

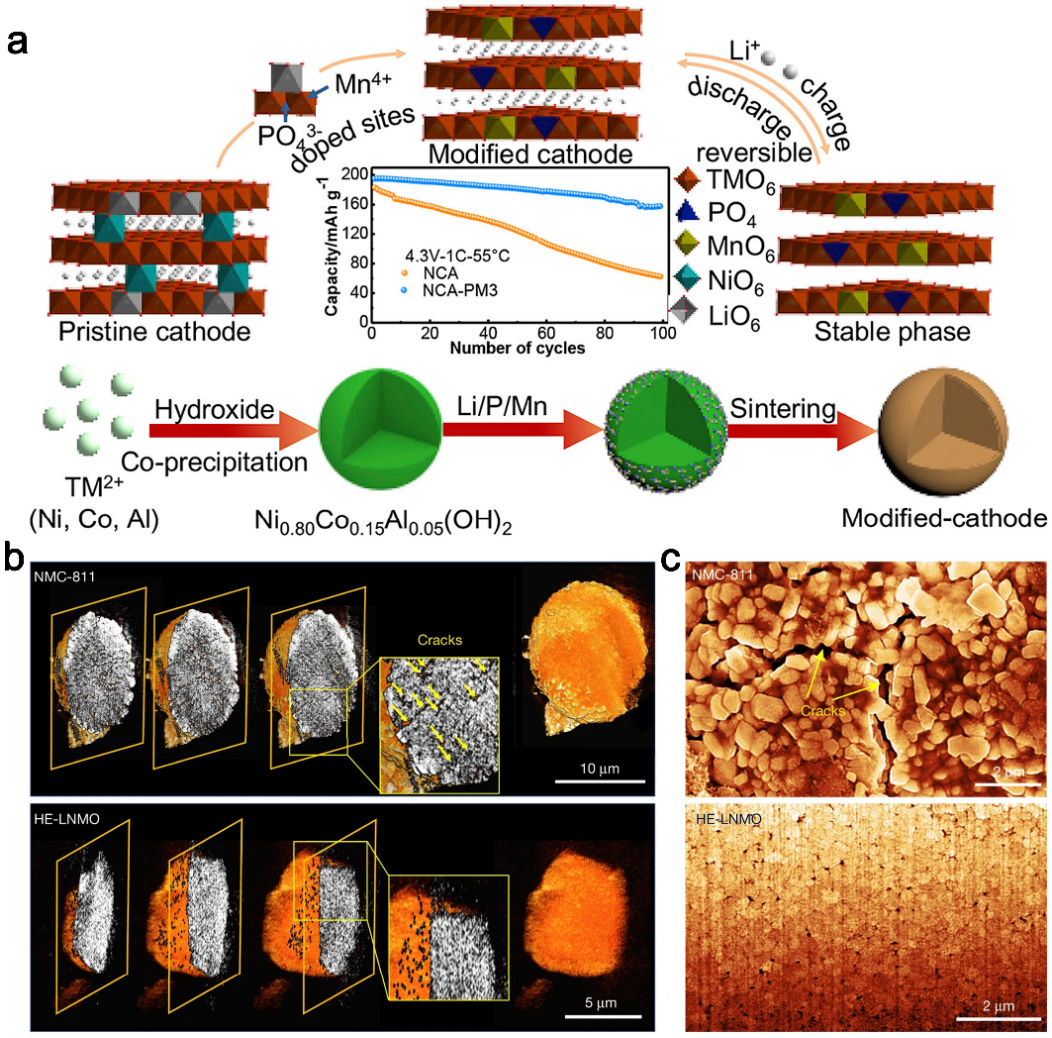


Figure 10. (**a**) Schematic illustration for the synthesis of modified material and the corresponding crystal structure [102]. Copyright 2019, Elsevier B.V. (**b**) Synchrotron-based TXM tomography showing the 3D structure of the NCM811 and HE-LNMO secondary particles after long-term cycling (100 cycles, 2.5–4.4 V (versus Li/Li), 1C). Substantial cracks (indicated by the arrows) are identified in cycled NCM811 (upper panel), whereas no evident cracks are observed in HE-LNMO (lower panel). (**c**) Representative cross-sectional SEM images of cycled NCM811 (upper panel) and HE-LNMO (lower panel) secondary particles [103]. Copyright 2022, Springer Nature.

3.2. Form and Microstructure Design

Given that the inherent anisotropic volume changes and associated mechanical stress in NCM811 are primary causes of secondary particle cracking and performance degradation, proactive management and release of internal stress through form and microstructural design have emerged as an effective strategy [106]. Distinct from compositional modification, this approach enhances mechanical stability through precise control of macroscopic morphology, internal compositional distribution, and grain architecture [107]. The objective of this strategy is to manage and dissipate the internal mechanical stresses induced by electrochemical cycling, thereby breaking the vicious cycle of chemo-mechanical coupled failure. By synthesizing single-crystal particles or designing polycrystalline aggregates with specific orientations (e.g., radially aligned), weak grain boundaries in conventional polycrystalline materials can be eliminated, or the stress distribution along grain boundaries can be guided uniformly. Such structural optimization directly acts on the mechanical response of the material, significantly alleviating localized stress concentrations caused by anisotropic variations in lattice parameters, which forms the physical basis for preventing the initiation and propagation of intra-particle cracks. Preserving particle integrity also effectively blocks the penetration pathways of electrolyte into the particle interior, thereby avoiding accelerated interfacial side reactions resulting from continuous exposure of fresh electrode surfaces.

3.2.1. Synthesis of Single Crystal

The absence of grain boundaries in single-crystal particles fundamentally eliminates stress concentration and intergranular crack initiation caused by anisotropic volume changes [108]. Without crack pathways for electrolyte penetration, the particle interior remains effectively protected from electrolyte-induced TM dissolution, oxygen loss, and rock-salt phase reconstruction, thereby preserving both structural integrity and electrochemical activity [109].

Single-crystal particles typically exhibit reduced specific surface area and lower surface energy, which mitigates interfacial side reactions. Their isotropic volume expansion/contraction imposes less strain on the crystal structure, contributing to suppressed H2–H3 phase transitions [108,110]. Single-crystal NCM811 is typically synthesized through molten-salt-assisted methods or high-temperature solid-state reactions [111]. By optimizing salt composition and synthesis temperature, single crystals with electrochemically stable (001) or (104) facets can be preferentially grown, enhancing interfacial stability at the source [110]. As shown in Figure 11a, Chen et al. developed a stable eutectic molten salt method that effectively reduces lithium volatilization [112]. The synthesized single-crystal Ni-rich cathode demonstrated exceptional structural and electrochemical stability. However, the molten-salt approach requires substantial salt usage and tedious washing steps, increasing process complexity and cost.

Alternatively, high-temperature solid-state methods promote primary particle fusion into single crystals through elevated sintering temperatures and extended durations. Jeff Dahn et al. systematically investigated the effects of Li/TM ratio, sintering temperature, precursor size, and sintering time on single-crystal Ni-rich cathode dimensions [113]. Their study recommends minimal temperature and Li/TM ratios to achieve optimal energy density. Nevertheless, high-temperature sintering often causes severe lithium loss and particle agglomeration, while excess lithium compensation may exacerbate Li/Ni cation mixing. As illustrated in Figure 11b, Xiao et al. discovered and systematically demonstrated Li_2O sublimation under ambient oxygen pressure, utilizing this phenomenon for synthesizing and regenerating high-performance single-crystal Ni-rich cathodes [114]. Through vapor-phase reaction between Li_2O and TM oxide precursors, they successfully obtained single-crystal NCM811 and NCM90. The resulting NCM811 single crystals exhibited exceptional cycling stability, providing a molten salt-free, simplified, and scalable synthesis route.

In summary, single-crystal design fundamentally resolves intergranular fracture and bulk degradation in NCM811 by eliminating grain boundaries. Future research should deepen the understanding of size effects and crystallographic orientation relationships, integrate single-crystal architecture with bulk doping and surface coating strategies, and develop environmentally benign, cost-effective synthesis pathways to enable scalable production.

3.2.2. Microstructural Engineering

Rational design of the internal microstructure in polycrystalline secondary particles can significantly enhance mechanical stability while preserving high tap density and favorable kinetics. Through strategies such as precursor morphology optimization and morphology-inducing dopants, radially aligned primary particles can be achieved, resulting in secondary particles with radial, rod-like, or platelet-like arrangements [115]. This radially aligned structure effectively transforms the random, inhomogeneous local stresses generated during cycling into more uniformly distributed circumferential hoop stresses. Such a stress distribution is more readily accommodated by

the material itself, thereby significantly suppressing the radial and transverse cracks responsible for particle fracture [116].

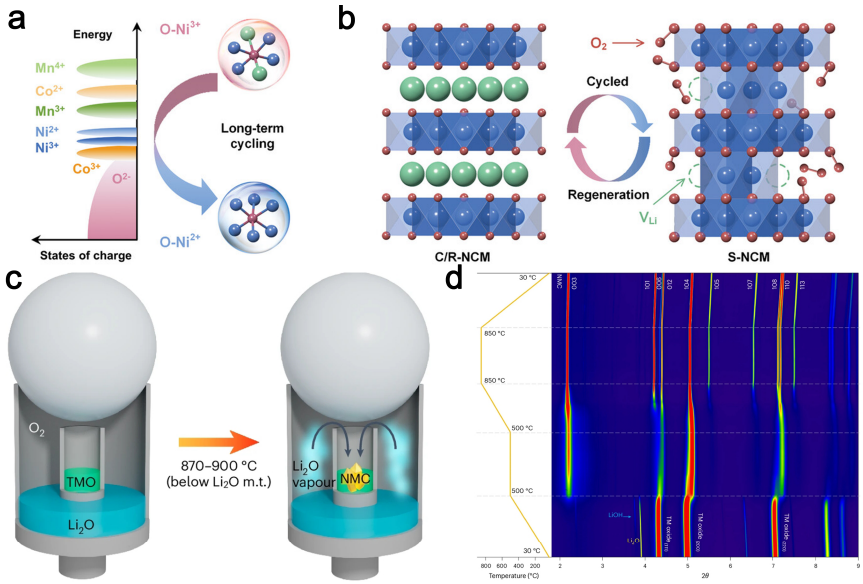


Figure 11. (**a**) Evolution of the Ni chemical state in NCA during the regeneration process and its corresponding band structure. (**b**) Schematic depicting the microscopic structure evolution from spent NCA (S-NCA) to regenerated NCA (R-NCA) [112]. Copyright 2025, Wiley-VCH. (**c**) Vapor study between Li_2O and TMO oxide precursors. (**d**) In situ XRD characterization (λ = 0.182 Å) tracks the reaction between TMO811 oxide precursor and Li_2O, following a procedure similar to that used for synthesizing NCM811 single crystals [114]. Copyright 2025, Springer Nature.

Xiang et al. prepared hydroxide precursors via a continuous coprecipitation method and investigated the effects of ammonia concentration and pH on the synthesis of primary and secondary particles [117]. Increased ammonia concentration preferentially promoted grain growth along the (001) plane and facilitated the construction of a radially oriented microstructure. Sun et al. proposed a multi-stage microstructure control strategy [118]. By designing a precursor with radially aligned needle-like primary particles and employing excess Al doping during lithiation, they utilized Al segregation at grain boundaries to inhibit grain coarsening, thereby preserving the optimal precursor morphology and concentration gradient in the final cathode material. This strategy effectively dissipated internal stress generated by severe lattice contraction/expansion during cycling, markedly suppressing the initiation and propagation of microcracks. As illustrated in Figure 12a, Xiang et al. precisely tailored a radially aligned microstructure in a Ni-rich cathode by combining coprecipitation and calcination [119]. By controlling ammonia concentration and pH during coprecipitation, they promoted the growth of primary particles along the (001) plane into a rod-like structure.

The core-shell structure represents a classic microstructural design, aiming to construct composite Ni-rich cathode particles comprising a “high-capacity core” and a “high-stability shell” [120]. However, the disparity in lattice constants and volume change rates between the two distinct phases during cycling can generate significant interfacial stress, ultimately limiting long-term cycling stability. Concentration gradient structures overcome this limitation. The continuous compositional transition eliminates sharp internal interfaces and ensures a gradual variation in lattice parameters, thereby converting intense interfacial stress concentration into a gently distributed internal stress gradient, effectively alleviating mechanical fatigue during phase transitions [121].

As shown in Figure 12b, Jiang et al. developed a Ni-rich cathode synergistically optimized by full concentration gradient (FCG) design and surface modification [122]. Gradient PO_4^{3-} doping suppressed TM ion interdiffusion during high-temperature sintering, stabilized the crystal structure, and reduced lattice oxygen release. The concentration gradient structure, Ni-rich in the core and manganese-rich/nickel-deficient at the surface, effectively mitigated stress concentration during charge/discharge, inhibiting microcrack formation and propagation. Sun et al. systematically studied the influence of calcination temperature on the physicochemical and electrochemical properties of a FCG Ni-rich cathode [123]. Excessively high calcination temperatures (e.g., 850 °C) led to coarsening of primary particles, disappearance of the composition gradient, and destruction of the radial alignment. The material calcined at 790 °C effectively retained the concentration gradient and radially aligned rod-like primary particle structure from the precursor, forming a Ni-rich core and nickel-deficient surface composition.

Yoo et al. achieved precise control over the composition gradient in Ni-rich cathode materials based on mathematical modeling and an automated reactor system [124]. Using time-dependent flow rate control functions, they independently manipulated the slope and curvature of TM concentration gradients within the precursor particles, forming a gradient structure with high nickel content internally and low nickel content externally.

In summary, microstructural engineering, through the construction of radially aligned primary particles and the design of composition gradient structures, enables effective regulation of internal stress distribution in NCM811 materials, providing potent solutions to their mechanical degradation. Future efforts should focus on developing more precise microstructural control processes to achieve accurate manipulation of primary particle size, orientation, and composition gradients. A deeper exploration of the intrinsic relationships between microstructure and electrochemical performance is needed to establish more comprehensive structure-property models. Concurrently, developing deeply integrated strategies that combine microstructural engineering with bulk doping and surface coating presents a highly promising research direction.

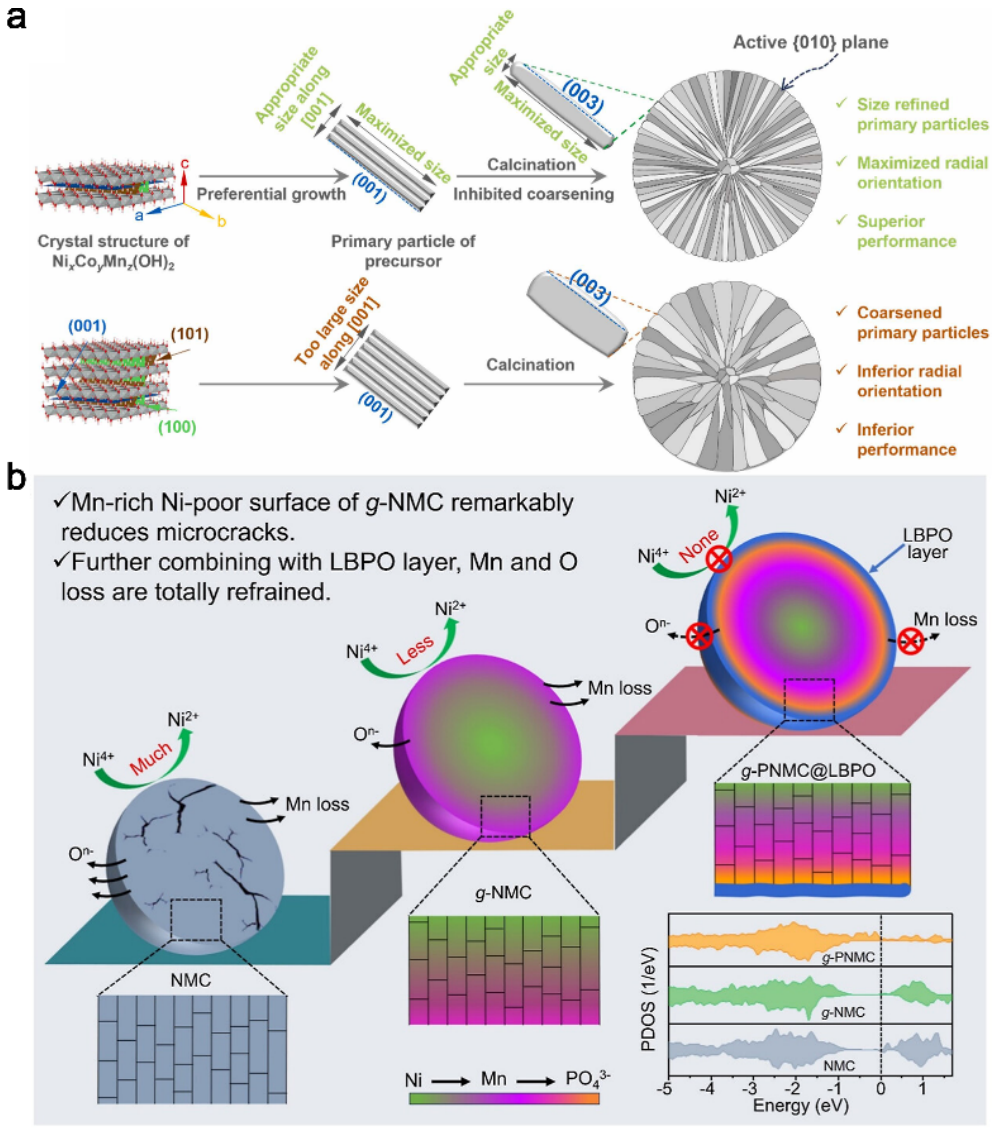


Figure 12. (**a**) Schematic diagram of the synthesis of Ni-rich cathode with different radially aligned microstructure during precursor precipitation and high temperature calcination [119]. Copyright 2014, Elsevier B.V. (**b**) Schematic illustration of the advantages of full concentration gradient Ni-rich cathodes, bottom right shows the calculated projected density of states of O 2p orbitals for NCM, gradient NCM (g-NCM), and gradient P-doped NCM (g-PNCM) after 90% Li-ion removal [122]. Copyright 2025, American Chemical Society.

3.3. Surface Coating

Detrimental interfacial side reactions are key drivers of structural degradation and capacity fading. Surface coating represents a direct interfacial engineering strategy, the core of which lies in isolating NCM811 cathode material from direct contact with the electrolyte [125,126]. This isolation suppresses interfacial side reactions,

limits TM dissolution, and enhances thermal stability, thereby significantly improving the structural integrity and interfacial compatibility of NCM811 [127]. A continuous coating layer can effectively block direct contact between the electrolyte and highly reactive sites on the electrode surface (such as residual lithium compounds and high-valence transition metal ions), thereby curbing the initiation of parasitic reactions.

3.3.1. Functional Design of Coating Materials

Various coating materials have been extensively investigated to improve the structural integrity and electrochemical properties of Ni-rich cathode [128]. Based on their physicochemical properties, coating materials are generally categorized as inert coatings, lithium-ion conductors, electronic conductors, and mixed conductors.

This section discusses two primary types: inactive coating substances without lithium storage capability, and coating candidates possessing lithium/electronic conductivity [129]. Inert coating materials typically include metal oxides (e.g., Al_2O_3, TiO_2, ZrO_2), fluorides (e.g., AlF_3, FeF_3, CaF_2), and phosphates (e.g., $AlPO_4$, $MnPO_4$) [130–133]. These materials function as physical barriers, isolating the cathode from direct electrolyte contact. As shown in Figure 13a,b, Wang et al. engineered a CeO_2 inert coating on the Ni-rich cathode material, effectively suppressing cathode-electrolyte interfacial side reactions [134]. Furthermore, benefiting from the excellent oxygen storage capacity of CeO_2, the release of lattice oxygen from the cathode was notably restrained, thereby enhancing the stability of the layered framework.

As illustrated in Figure 13c, Zeng et al. employed a combined strategy of Se doping and $FeSe_2/Fe_2O_3$ dual-modification interface engineering to significantly enhance the structural stability and cycle life of NCM811 cathodes under high voltage [135]. Se doping occupies oxygen vacancies and forms stable O-TM-Se bonds, effectively suppressing lattice oxygen release and mitigating structural distortion. The $FeSe_2/Fe_2O_3$ heterostructure creates a built-in electric field that enhances interfacial charge transfer, while $FeSe_2$ promotes Li^+ diffusion and consumes active oxygen, generating protective SeO_2 and Fe_2O_3. The Fe_2O_3 coating acts as an electrostatic shielding layer, inhibiting HF corrosion and oxygen anion outward migration, further enhancing interfacial stability. Sun et al. constructed a uniform $LiAlO_2$ coating on the NCM811 surface through acid etching and polyvinylpyrrolidone cross-linking [136]. This coating not only served as a physical barrier against electrolyte contact but also, acting as a lithium-ion conductor, suppressed Li^+/Ni^{2+} cation mixing and hindered lattice oxygen release. Bresser et al. coated NCM811 cathode particles with poly (arylene ether sulfone) functionalized with lithium phosphate, effectively suppressing detrimental interfacial side reactions during storage and cycling [137]. Furthermore, this polymer coating facilitated the formation of a stable CEI, significantly improving the rate capability and cycle life of NCM811.

Electronically conductive polymer coatings can effectively enhance surface charge transfer kinetics and are easily applied as uniform, continuous layers on NCM811 particles. As illustrated in Figure 13d, Chen et al. utilized oxidative chemical vapor deposition to apply a conformal poly(3,4-ethylenedioxythiophene) (PEDOT) protective layer on a Ni-rich cathode [138]. The PEDOT coating simultaneously promoted the transport of both lithium ions and electrons. It also effectively suppressed the detrimental phase transition from the layered structure to spinel and rock-salt phases and alleviated both intergranular and intragranular mechanical cracking.

Hybrid coatings, which leverage the synergistic effects between different functional materials, offer a promising route to enhance the overall performance of Ni-rich cathodes. As depicted in Figure 13e, Zeng et al. proposed a dual-modified LiF/FeF_3 hybrid coating on the NCM811 cathode [139]. This hybrid coating effectively suppressed intergranular cracks, increased the formation energy of oxygen vacancies, and enhanced Li^+ migration rates. Wang et al. synthesized a high-modulus coating composed of $Li_{1.5}Al_{0.5}Ti_{1.5}(PO_4)_3$ (LATP) and halloysite nanotubes (HNTs) on a Ni-rich cathode surface [140]. This hybrid coating effectively mitigated lattice volume changes. Furthermore, the fast Li^+ conductor within the hybrid coating accelerated Li^+ diffusion kinetics.

In summary, surface coating significantly enhances the interfacial stability and electrochemical performance of NCM811 cathodes through mechanisms including physical isolation, chemical stabilization, and interface conduction regulation. The current design philosophy for coating materials has evolved from merely providing a physical barrier towards active regulation and optimization of the interfacial microenvironment. Future efforts should focus on in-depth investigation of the dynamic evolution mechanisms of coating materials during cycling and their interaction with the bulk structure. Integrating coating with doping and structural design to develop multifunctional composite coatings represents a promising direction for achieving comprehensive optimization from the interface to the bulk.

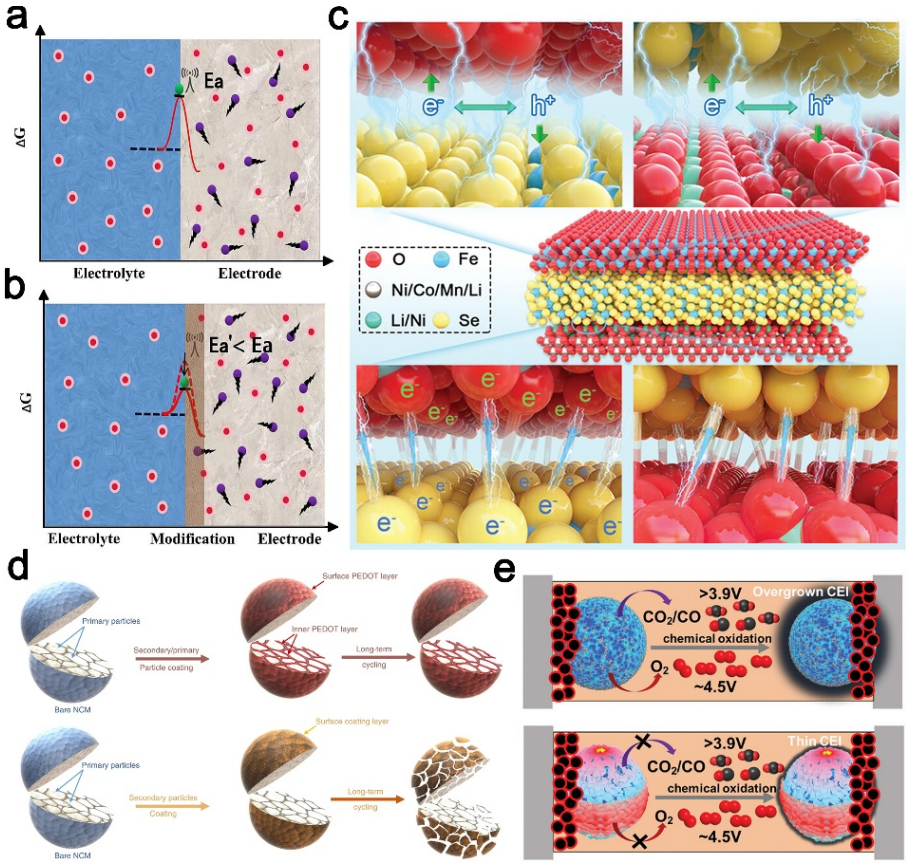


Figure 13. (**a**,**b**) Schematic diagram comparing the surface activation energy barrier before and after modification [134]. Copyright 2025, Elsevier B.V. (**c**) Schematic of the constructed heterointerfaces in Se-NCM811/$FeSe_2$ and $FeSe_2$/Fe_2O_3 composites [135]. Copyright 2024, Wiley-VCH. (**d**) An illustration of the structural stability of both secondary/primary particle coating and secondary particle coating only after long-term cycling. The oCVD process led to conformal PEDOT coating on both secondary and primary particles, resulting in no particle cracking after a long cycle life, while secondary particle coating only by conventional processes resulted in particle cracking after a long cycle life [138]. Copyright 2019, Springer Nature. (**e**) Schematic diagrams comparing the evolution of the CEI on NCM811 and LiF/FeF_3-modified NCM electrodes during prolonged cycling [139]. Copyright 2023, Wiley-VCH.

3.3.2. Coating Processes

The performance of the coating depends largely on its microstructure, which is precisely determined by the preparation process. Different coating processes directly determine the continuity, uniformity, thickness, and adhesion strength of the coating layer to the Ni-rich cathode surface. As illustrated in Figure 14a, Li et al. constructed a cobalt-boron metallic glass layer with dual coating and penetrating functionality via a room-temperature liquid-phase reactive wetting process [7]. This technique not only achieved complete coverage on secondary particle surfaces but also enabled spontaneous infiltration into the grain boundaries between primary particles through reactive wetting, forming a super conformal, zero-contact-angle coating layer. The strong selective interfacial bonding between Co_2B and surface oxygen atoms formed stable Co-O and B-O covalent bonds, significantly reducing surface oxygen activity and suppressing lattice oxygen release. As shown in Figure 14b, Zhuang et al. prepared a conductive lithium borate glass-coated NCM811 cathode through a simple dry process [141]. The LOBO coating exhibited high ionic conductivity and low electronic conductivity, facilitating Li^+ transport across the interface while suppressing decomposition of the solid electrolyte. Simultaneously, the coating stabilized the cathode lattice structure and promoted the formation of a uniform, dense CEI. Brezesinski et al. developed a wet-coating strategy based on pre-synthesized nanoparticles (NPs) [142]. This process formed a bilayer structure on the Ni-rich cathode surface, comprising an outer monolayer of ZrO_2 nanoparticles and an inner layer of carbonaceous/lithium carbonate species. This coating achieved uniform and thickness-controllable coverage on the cathode particle surface, significantly suppressing interfacial side reactions. Zhao et al. employed atomic layer deposition (ALD) to construct an ultrathin, uniform TiO_2 coating layer [143]. The ALD technique enabled precise control over the TiO_2 coating thickness (1–5 nm) and its homogeneity. The TiO_2 coating effectively inhibited the formation of intergranular cracks. Zhang et al. utilized magnetron sputtering to fabricate

an amorphous Li_3PO_4 coating on a Ni-rich cathode surface [144]. This coating effectively enhanced the high-temperature conductivity and electrochemical stability of the cathode.

In summary, coating preparation technologies have evolved from simple physical mixing towards precise manipulation of coating microstructure. Advanced techniques, ranging from room-temperature liquid-phase reactive wetting to atomic layer deposition, demonstrate significant advantages in achieving complete coverage, precise thickness control, and grain boundary penetration. Future development should focus on creating simpler, lower-cost, and highly precise preparation processes to facilitate the industrial application of high-performance coatings.

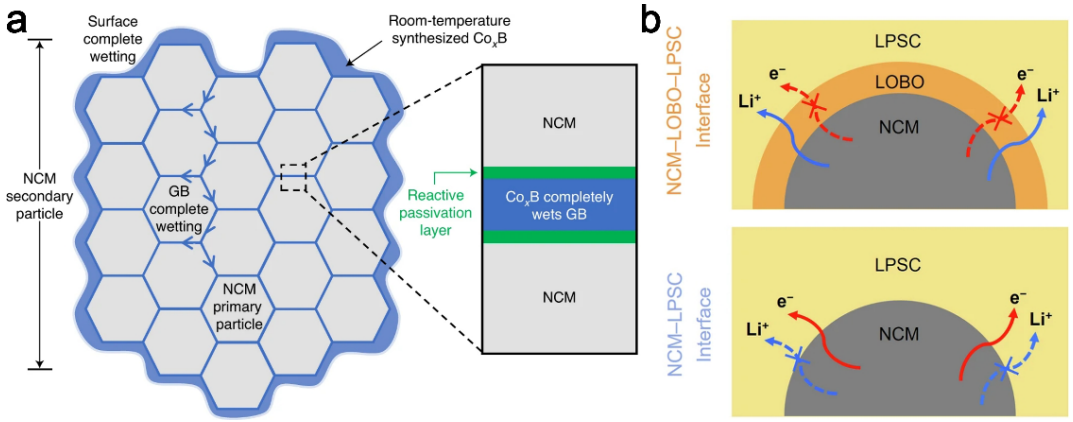


Figure 14. (**a**) Schematic of a modified microstructure featuring a Co_xB coating uniformly covering the NCM secondary particle surface [7]. Copyright 2021, Springer Nature. (**b**) Illustration of the interfaces between NCM and two solid electrolytes: LOBO and LPSC [141]. Copyright 2025, Springer Nature.

3.4. Electrolyte and Additive Engineering

Electrolyte and additive engineering, through molecular design and component optimization, enables the in-situ and dynamic construction of stable interfaces at the electrode surfaces. This strategy leverages the selective redox characteristics of functional additive molecules, allowing them to react preferentially over the base solvents at the electrode surface, thereby dominating the formation of a stable cathode-electrolyte interphase (CEI). This effectively suppresses subsequent continuous electrolyte decomposition and transition metal dissolution. Simultaneously, certain additive molecules act as scavengers, capable of specifically chelating or neutralizing aggressive species generated in the electrolyte, such as hydrofluoric acid and reactive oxygen radicals, fundamentally disrupting the mutually catalytic chain reactions of various interfacial side reactions. Furthermore, innovative systems like localized high-concentration electrolytes enhance the oxidation stability of the electrolyte system at a fundamental level by restructuring the solvation sheath of lithium ions and reducing the number of free solvent molecules.

3.4.1. Functional Additives

The introduction of functional additives into the electrolyte represents one of the most cost-effective, efficient, and industrially scalable strategies for enhancing the interfacial stability of NCM811 cathodes. Based on their mechanisms of action, these additives can generally be categorized as follows: Firstly, film-forming additives preferentially undergo oxidative decomposition or specific adsorption on the cathode surface, thereby guiding the formation of a robust and stable CEI, which improves the interfacial stability and electrochemical performance of NCM811. Secondly, scavengers and stabilizers effectively eliminate HF, reactive oxygen species generated by lattice oxygen release from NCM811 under high voltage, and selectively chelate dissolved TM ions. Furthermore, multifunctional additives and synergistic combinations have been developed.

The strategic selection of additives containing characteristic functional groups (e.g., B, F, N, P) facilitates the formation of a stable CEI on Ni-rich cathode surfaces, thereby suppressing the continuous decomposition of ester-based solvents. He et al. employed lithium difluorophosphate (LiDFP) as a film-forming additive, which significantly enhanced cycling stability and capacity retention [145]. The decomposition products of LiDFP strongly adsorb onto and cover the Ni active sites on the cathode surface, blocking hydrogen abstraction pathways. This effectively inhibits H_2 evolution and TM dissolution. Ma et al. introduced heptafluorobutyric anhydride (HFA) to promote the formation of a compact CEI [146]. Concurrently, HFA enhances separator wettability, increases lithium-ion flux, suppresses lithium dendrite growth, and promotes uniform lithium deposition by facilitating lithium-ion desolvation. As shown in Figure 15a,b, Lai et al. developed a film-forming additive,

hexabutylcyclohexane-1,2,3,4,5,6-hexaimide (HBCHHI) [147]. Benefitting from its high HOMO and low LUMO energy levels, HBCHHI undergoes preferential oxidation at the cathode and reduction at the anode, thereby participating in the construction of the interface layer. Certain film-forming additives can induce electrolyte components to form stable electrode-electrolyte interphase layers, thereby enhancing the long-term cycling stability of Ni-rich cathodes. Shao et al. proposed a strategy for constructing a stable CEI via in situ polymerization [148]. Using aluminum isopropoxide (AIP) as an initiator and with the synergy of Al^{3+}, ring-opening polymerization of ethylene carbonate was triggered, forming polycarbonate-rich polymer chains. The resulting polymers, along with Al^{3+} derivatives (e.g., Al_2O_3 and AlF_3), co-assemble into a uniform, dense CEI layer approximately 7 nm thick. This CEI layer effectively prevents further electrolyte decomposition, TM dissolution, HF attack, and inhibits phase transitions and particle cracking in the NCM material under high voltage. As illustrated in Figure 15c, Ma et al. proposed an additive, *N*,*N*-dimethyl-4-(4,4,5,5-tetramethyl-1,3,2-dioxaborolan-2-yl)aniline (DMPATMB), designed to scavenge HF in the electrolyte and suppress interfacial side reactions [149]. This additive forms a thin and uniform CEI on the cathode surface while scavenging HF, thereby disrupting the vicious cycle of HF-induced interfacial corrosion and electrolyte decomposition. This enhances the structural integrity of the Ni-rich cathode material.

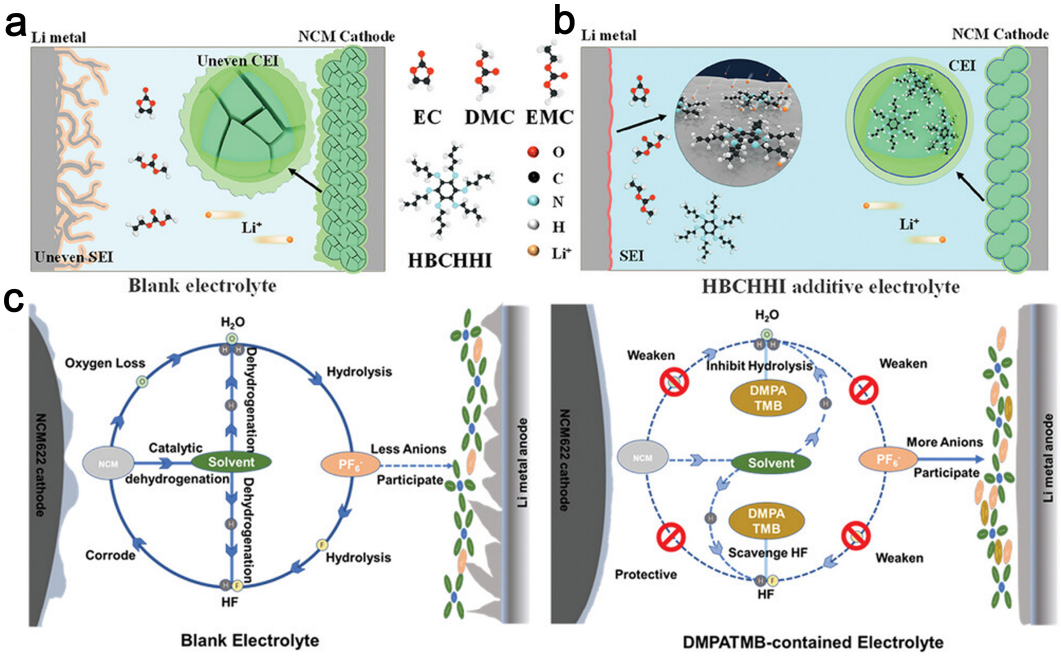


Figure 15. (**a**,**b**) The protection mechanism for the solid-electrolyte interphase and cathode-electrolyte interphase in (**a**) a blank electrolyte and (**b**) an electrolyte containing HBCHHI [149]. Copyright 2023, Wiley-VCH. (**c**) Schematic comparing the vicious cycle of side reactions in a blank electrolyte versus the effective protection offered by a DMPATMB-containing electrolyte for lithium metal batteries (LMBs). Dashed lines represent suppressed reactions [148]. Copyright 2023, Wiley-VCH.

Based on the Fukui function analysis, Cao et al. identified 4-(trifluoromethyl)thiobenzamide (TFSBN) as a multifunctional electrolyte additive [150]. The TFSBN molecules undergo preferential oxidation over solvent molecules at the cathode interface, forming a stable CEI rich in inorganic components such as Li_2S, Li_2SO_4, Li_3N, and LiF. Through strong electrostatic interactions, TFSBN preferentially adsorbs on the NCM811 cathode surface, thereby modifying the lithium-ion solvation structure at the interface. This promotes the formation of an inorganic-rich interphase and enhances lithium-ion diffusion kinetics. As shown in Figure 16, Lee et al. developed nano-Si_3N_4 as a multifunctional electrolyte additive that enables long-term cycling stability for NCM811 under high-voltage operation [151]. This additive facilitates the construction of a composite SEI on the anode, characterized by a LiF-rich outer layer and a fast Li^+ conducting inner layer rich in $Li_3N/Li_4Si_3N_4$. Concurrently, it stabilizes the cathode structure by suppressing the hydrogen transfer reaction of ethylene carbonate (EC) at high voltage and scavenging HF from the electrolyte.

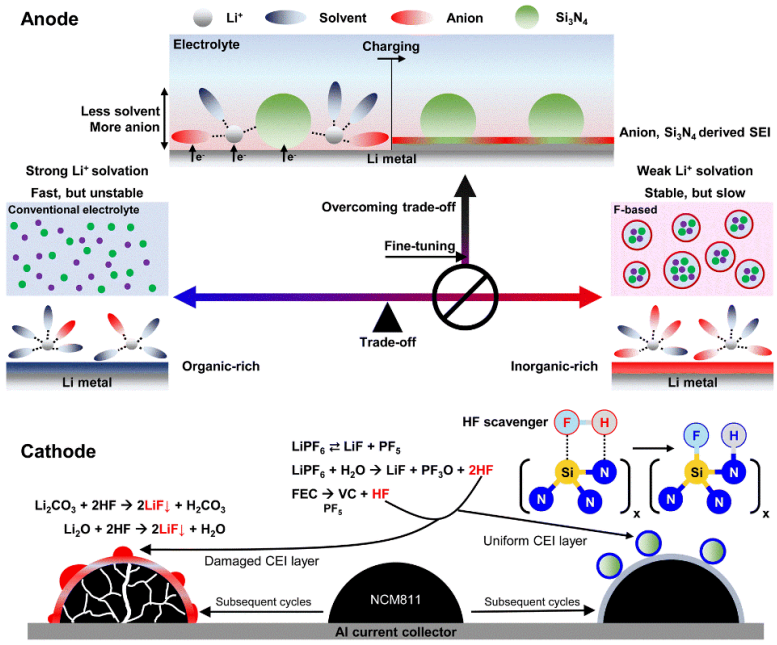


Figure 16. Design logic for introducing a nano-Si_3N_4 additive for concurrent electrode-electrolyte interface engineering. Conventional fluorinated electrolytes, including HCEs, LHCEs, and fluorinated solvents, exhibit a highly weak Li^+ solvation environment. On the other hand, the nano-Si_3N_4 additive facilitates slightly weaker Li^+ solvation compared to the Blank, resulting in a minor ionic conductivity decrease. It will be mitigated by SEI layer engineering, which involves the alloying and conversion reaction of nano-Si_3N_4 with Li metal [151]. Copyright 2025, The Royal Society of Chemistry.

Electrolyte additives, through rational molecular design, provide the most economically efficient solution for constructing stable electrode-electrolyte interfaces. The evolution from single-function film-forming additives to multifunctional additive systems capable of simultaneously scavenging detrimental species and modulating solvation structures has enhanced the interfacial stability and cycling longevity of NCM811 under high-voltage operation. Further investigation remains crucial to elucidate the dynamic reaction pathways of additive molecules at electrode interfaces and the formation mechanisms of interphase layers, thereby enabling better compatibility with Ni-rich cathode materials.

3.4.2. Localized High-Concentration Electrolyte

High-concentration electrolytes (HCEs) significantly enhance the stability of electrode/electrolyte interfaces by modifying the primary solvation sheath structure of Li^+. However, conventional HCEs suffer from high viscosity, elevated cost, and poor wettability. To overcome these challenges, localized high-concentration electrolytes (LHCEs) have been designed as a promising approach. The design strategy involves introducing a substantial amount of inert diluent, which does not strongly coordinate with Li^+, into a high-concentration lithium salt solution with its primary solvent. These inert diluents typically possess low dielectric constants and minimally participate in Li^+ solvation. Their primary function is to reduce the overall viscosity of the electrolyte, thereby improving wettability and ionic conductivity. Crucially, at the molecular scale, because the coordination ability of the primary solvent molecules with Li^+ far exceeds that of the diluent, the structure of the primary Li^+ solvation sheath remains similar to that in HCEs, predominantly comprising anions and a small number of primary solvent molecules. As shown in Figure 17a–d, Serizawa et al. reported the introduction of the hydrofluoroether 1,1,2,2-tetrafluoroethyl-2,2,3,3-tetrafluoropropyl ether (HFE) as a diluent into a high-concentration electrolyte [152]. When the salt concentration was diluted to 1 M, the electrolyte viscosity decreased to 3 mPa s. Zhang et al. utilized the inert diluent bis(2,2,2-trifluoroethyl) ether (BTFE) to formulate an LHCE from an HCE, simultaneously achieving high compatibility with the lithium metal anode and exceptional stability with the high-voltage NCM811 cathode [153]. The inert diluent BTFE does not coordinate with the lithium salt, thus preserving the specific solvation structure formed between Li^+, the solvent, and FSI^- anions from the HCE at the molecular scale. This maintains the localized HCE environment, ensuring its intrinsic high stability. Xu et al. added 1,1,2,2-tetrafluoroethyl-2,2,3,3-tetrafluoropropyl ether (TTE) as a diluent to an HCE composed of lithium bis(fluorosulfonyl)imide (LiFSI) and 1,2-dimethoxyethane (DME) at a molar ratio of 1:1.2, forming an LHCE [154]. This ether-based LHCE exhibited excellent high-voltage stability, significantly extending the cycle life of the

NCM811 cathode material under high voltage. Zhang et al. prepared a flame-retardant LHCE by mixing triethyl phosphate/bis(2,2,2-trifluoroethyl) ether (TEP-BTFE) with LiFSI [155]. The TEP-BTFE formulation retained the specific Li^+ solvation structure and improved interfacial reaction kinetics. As illustrated in Figure 17e, Zhao et al. developed a dual-salt localized high-concentration electrolyte based on sulfolane/ethyl acetate [156]. By introducing a dual-salt system (LiTFSI and LiDFOB), the inert diluent HFE, and 10 wt% fluorocarbonate (FEC), they constructed a multifunctional electrolyte system enabling stable charge/discharge across a wide temperature range and under high voltage. The HFE dilution maintained the localized high concentration. LiDFOB preferentially formed a stable CEI rich in B-F and B-O components on the cathode surface, while FEC synergistically enhanced interfacial uniformity and oxidation resistance, effectively suppressing aluminum foil corrosion and TM dissolution. As depicted in Figure 17f, Zhang et al. developed an LHCE based on sulfolane (SL) and the diluent TTE for NCM811 cathodes [157]. The TTE diluent promoted the formation of a localized high-concentration solvation structure dominated by contact ion pairs and aggregate clusters for LiTFSI, reducing free solvent molecules and suppressing side reactions. Furthermore, LiFSI and TTE underwent synergistic decomposition on the cathode surface, forming a uniform and dense inorganic-organic composite CEI that effectively inhibited electrolyte decomposition.

LHCE successfully combine the practical advantages of low viscosity, high ionic conductivity, and enhanced wettability with the fundamental capability of HCE to form stable anion-derived electrode-electrolyte interphases. Through rational selection of primary solvent and diluent combinations, LHCE facilitate the formation of robust anion-derived interfacial layers on NCM811 cathode surfaces, effectively suppressing interfacial side reactions and structural degradation under high-voltage operation. Future research should focus on quantitatively elucidating the influence of different solvent/diluent combinations on Li^+ solvation structures and further clarifying the precise mechanistic role of diluents in the interphase formation process.

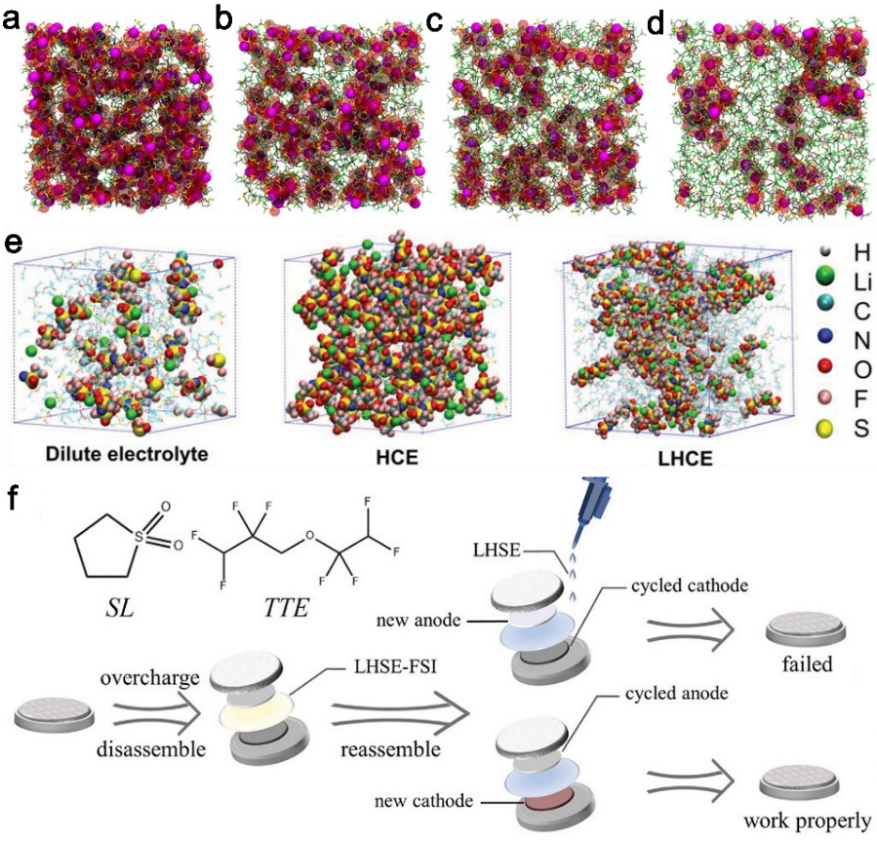


Figure 17. (**a**–**d**) Snapshots of the MD simulations of (**a**) SL-based HCEs and those of LHCEs at a c of (**b**) 2.06, (**c**) 1.57, and (**d**) 1.07 mol·dm^{-3}. Color code: purple, lithium ion; gray, carbon; red, oxygen; yellow, sulfur; blue, nitrogen; green, fluorine. The red transparent volume represents the surface of oxygen atoms in the first coordination shell of Li^+ ions [152]. Copyright 2023, American Chemical Society. The simulations and schematics demonstrate that LHCEs maintain a beneficial local solvation structure, enabling the formation of stable anion-derived interphases. (**e**) Molecular dynamics (MD) simulation results of dilute electrolyte (TE-1m-LiTFSI), HCE (TE-5m-LiTFSI), and LHCE (TEH-1.1m-LiTFSI) [156]. Copyright 2021, Wiley-VCH. (**f**) Schematic diagram of the reassembly process for preparing test cells [157]. Copyright 2024, Wiley-VCH.

3.4.3. Novel Solvent and Lithium Salt

Conventional electrolytes predominantly comprising carbonate-based solvents offer advantages such as high ionic conductivity, suitable viscosity, and strong dissociative ability. However, to further enhance the stability of NCM811 at high-voltage, novel solvents including fluorinated solvents, sulfones, ethers, and nitriles have been successively developed. As illustrated in Figure 18a, Liu et al. formulated a fluorinated electrolyte using $LiPF_6$ as the lithium salt, with bis(2,2,2-trifluoroethyl) carbonate (BTC) and 1H,1H,5H-perfluoropentyl-1,1,2,2-tetrafluoroethylether (HFE) as solvents [158]. They further introduced the high-polarity co-solvent sulfolane (SL) and LiDFOB, implementing a co-solvent occupancy strategy. The highly polar and oxidation-resistant SL, due to its stronger binding energy with Li^+, successfully occupies the innermost solvation sheath, thereby enhancing the overall oxidation stability of the electrolyte. The stronger interaction between SL and $DFOB^-$ anions ensures the effective enrichment and preferential oxidative decomposition of $DFOB^-$ at the NCM811 cathode interface. This process constructs an anion-derived CEI rich in inorganic components such as LiF, B-F, and B-O. As shown in Figure 18b, Coskun et al. developed a targeted functionalization strategy for the cyclic ether solvent 1,3-dioxolane (DOL), creating 4-(trifluoromethyl)-1,3-dioxolane (TFDOL) with a trifluoromethyl substituent, which significantly improved the oxidation stability and interfacial compatibility [159]. Introducing the strong electron-withdrawing-CF_3 group reduces the electron density on the oxygen atoms of the DOL ring, effectively suppressing its electrochemical ring-opening polymerization at high voltages and elevating the oxidation stability limit from 3.5 V to 5.0 V. The NCM811 cathode using this electrolyte exhibited 89% capacity retention after 100 cycles. Future development of novel solvents should focus on establishing structure-property relationships to guide the molecular design of solvents with targeted functionalities, such as enhanced oxidation stability and the ability to form favorable interphases.

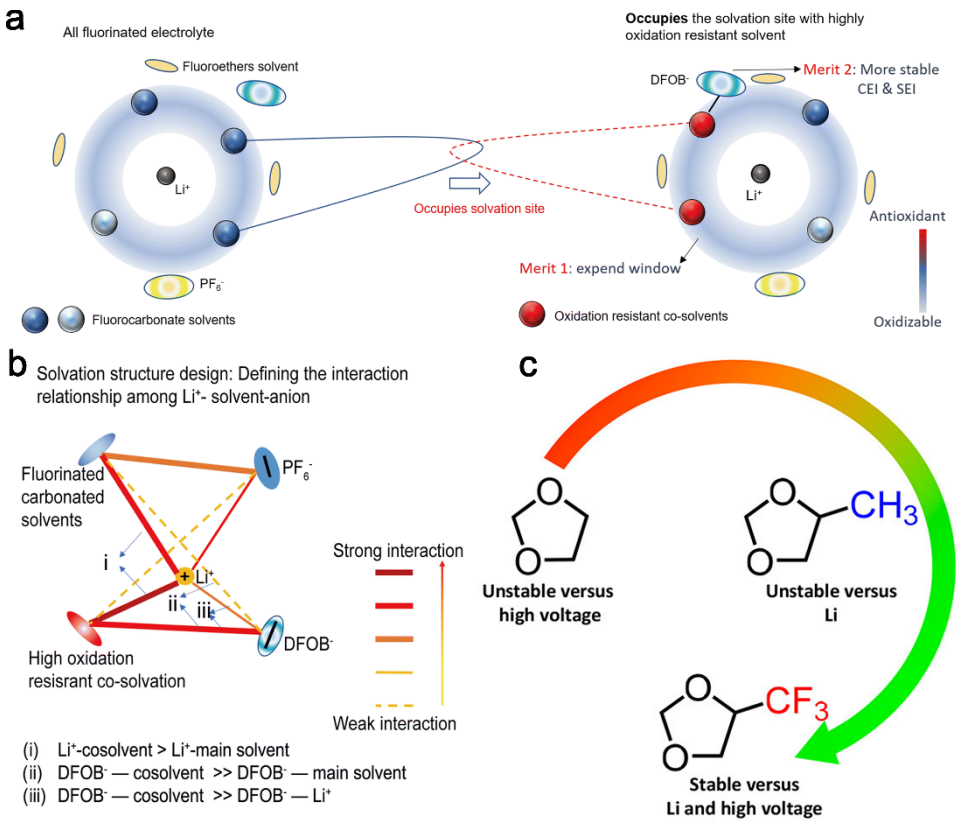


Figure 18. (**a**) Solvation site occupation strategy using auxiliary solvents. (**b**) Energy ranking of Li^+-solvent-anion pairwise interactions in different electrolytes [158]. Copyright 2024, The Royal Society of Chemistry. (**c**) MDOL and TFDOL is developed by introducing methyl and trifluoromethyl groups to the ethyl moiety of DOL [159]. Copyright 2023, American Chemical Society.

The poor chemical and thermal stability of $LiPF_6$ limits its application in high-voltage ternary lithium-ion batteries. New lithium salts that have been extensively researched include lithium bis(fluorosulfonyl)imide (LiFSI), lithium bis(trifluoromethanesulfonyl)imide (LiTFSI), lithium difluoro(oxalato)borate (LiDFOB), and lithium difluorobis(oxalato)phosphate (LiDFBOP). However, in practical applications, besides cost constraints, these lithium salts have their respective limitations and are currently typically used as additives or in blended salt

systems. Dahn et al. developed a dual-salt liquid electrolyte leveraging the synergistic effect of LiDFOB and $LiBF_4$ [160]. The decomposition products of LiDFOB and $LiBF_4$ complement each other, constructing a stable SEI with both mechanical strength and interfacial toughness. At the cathode under high voltage, LiDFOB oxidatively decomposes prior to the solvents, forming a stable CEI. $LiBF_4$ not only participates in CEI formation but also suppresses excessive decomposition of LiDFOB and associated gas evolution side reactions.

Novel solvents and lithium salts effectively suppress interfacial side reactions and structural degradation in NCM811 cathodes under high-voltage conditions through mechanisms involving the modulation of Li^+ solvation structures and the induction of robust, anion-derived interphases. However, solvents such as sulfones and nitriles exhibit poor compatibility with graphite anodes, making them unlikely to replace carbonate-based solvents in the foreseeable future. Given that no single novel lithium salt currently surpasses $LiPF_6$ in overall comprehensive performance, exploring blended lithium salt systems represents a more viable strategy at present. Concurrently, further investigation into the regulatory mechanisms of ionic liquids on both solvation structures and the interfacial composition of NCM811 cathodes is warranted.

3.5. Functionalized Separator and Solid-State Electrolyte

Functionalized separators can effectively enhance the cycling stability of cathode materials by selectively adsorbing corrosive species (e.g., HF and dissolved TM ions), homogenizing the Li^+ flux distribution, and actively participating in the formation of a stable CEI, thereby suppressing interfacial side reactions. Solid electrolytes physically eliminate the solid-liquid interface and all associated side reactions. Their inherent high mechanical strength also exerts a constraining effect on the volume changes of the active electrode materials, thereby inhibiting physical degradation of the electrode structure.

3.5.1. Functionalized Separator

Traditional polyolefin separators mainly play a passive role in electronic insulation and preventing positive and negative electrode contact in lithium ion batteries, but have limited influence on the interface side reactions and ion transport kinetics of the battery. Therefore, the functional design of the separator to give it the ability to actively regulate the interface and enhance safety is one of the core strategies to improve the performance of NCM811 batteries.

Through deliberate design of microstructure and surface chemical sites, separators can be engineered to ensure efficient lithium-ion conduction while simultaneously blocking TM ions shuttling and actively scavenging HF, thereby stabilizing the electrode-electrolyte interface. As shown in Figure 19a, He et al. fabricated an ultrathin (12 μm) bilayer functional separator by coating a polyvinylidene fluoride (PVDF) layer onto a polyimide (PI) substrate [161]. The imide rings provide abundant HF coordination sites, enabling effective HF adsorption through the formation of C=O···H-F hydrogen bonds. This functional separator effectively suppressed structural degradation and detrimental interfacial side reactions in NCM811, significantly enhancing its cycling stability. Lee et al. developed a functional separator by coating 3-glycidyloxypropyl trimethoxysilane (GPTMS)-modified self-assembled chiral nematic liquid crystalline cellulose nanocrystal (LC-CNC) onto a polyethylene (PE) separator [162]. The highly ordered nanoporous channels within the LC-CNC layer promote uniform lithium deposition. Furthermore, the GPTMS functional groups in the LC-CNC layer effectively chelate dissolved TM ions from the NCM811 cathode, inhibiting detrimental interfacial reactions and enhancing cathode structural stability. Additionally, Silvia Bodoardo et al. incorporated a molybdenum disulfide/polyaniline interlayer into lithium-sulfur batteries to adsorb polysulfides, and this concept of introducing an independent intermediate layer also holds considerable reference value [163].

As illustrated in Figure 19b, Guo et al. developed a tandem-architecture functional separator by modifying both sides of a polypropylene substrate with a cyanide-functionalized covalent organic framework (COF) and SnF_2, respectively [164]. On the cathode side, the groups in the COF induce the formation of a stable CEI through adsorption/coordination with TM ions, effectively suppressing TM dissolution and irreversible phase transitions. Simultaneously, the SnF_2 layer on the anode side constructs a stable SEI composed of LiF and Li-Sn alloys via in situ conversion reactions. As shown in Figure 20c, He et al. prepared amino-modified UIO-66 zirconium metal-organic frameworks (MOFs) as a coating for functional separators [165]. This functional separator exhibits high efficiency in scavenging trace water molecules from the electrolyte, fundamentally suppressing HF-induced corrosion of the NCM811 cathode.

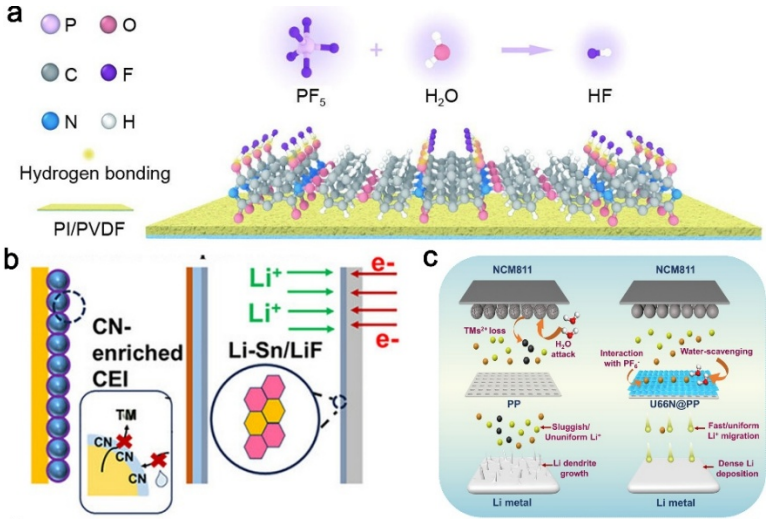


Figure 19. (**a**) Schematic mechanism by which a PI/PVDF composite separator inhibiting the capacity decay of NCM811 [161]. Copyright 2024, Elsevier B.V. (**b**) Schematic diagram of regulating dual-interface properties through a tandem-structured modification [164]. Copyright 2025, Wiley-VCH. (**c**) Schematic illustrating the role of amino-functionalized MOFs in removing trace water promoting Li salt dissociation [165]. Copyright 2025, Elsevier B.V.

Transitioning from passive isolation to active interfacial regulation, controlling the formation of CEI/SEI layers represents a core strategy in functional separator design. In another study (Figure 20a), Chi et al. functionalized a separator using two solid-state electrolytes, $Li_{6.4}La_3Zr_{1.4}Ta_{0.6}O_{12}$ (LLZTO) and $Li_{1.3}Al_{0.3}Ti_{1.7}(PO_4)_3$ (LATP) [166]. The LATP layer coated on the cathode side effectively captures dissolved TM ions from the Ni-rich cathode, thereby enhancing the structural stability of NCM811. Meanwhile, the LLZTO layer on the anode side selectively adsorbs FSI- anions, facilitating the desolvation process of Li^+ and consequently significantly improving lithium-ion transport kinetics across the interface. Park et al. developed a molecularly functionalized separator by introducing polar functional groups onto a conventional polyolefin separator [167]. On the cathode side, the separator stabilizes PF_5 via polar interactions, inhibiting its hydrolysis into HF and thereby mitigating HF-induced corrosion, phase transition, and TM dissolution in NCM811 cathodes. As shown in Figure 20b, Zhang et al. constructed a functional separator by impregnating lithium nitrate into hollow mesoporous silica composites and coating this onto a commercial separator [168]. The lithium nitrate preferentially undergoes oxidative decomposition on the NCM811 cathode, generating a thin and uniform CEI that effectively suppresses electrolyte side reactions. Functional separators can also stabilize the NCM811 cathode interface through physical regulation without directly participating in CEI formation reactions. Wei et al. proposed a dielectric enhancement strategy induced by F-C-O coordination [169]. A PVDF-GO polymer coating with high dielectric constant effectively promotes lithium-ion migration at the CEI while repelling anions from approaching the cathode, thereby optimizing the ionic distribution at the interface. This functional separator fundamentally suppresses PF6- decomposition and subsequent HF generation.

Heat-resistant functional separators effectively mitigate the low melting point and poor thermal dimensional stability of commercial polyolefin separators, thereby significantly reducing the thermal runaway risk of NCM811 batteries. Wu et al. fabricated a zirconia nanolayer-coated PI composite separator via a polar adsorption and hydrolysis strategy [170]. The ZrO_2 nanolayer forms a cross-linked core-shell structure on the PI surface, endowing the separator with exceptional mechanical strength and superior thermal stability. Liu et al. prepared a PI/SiO_2 separator with a core-shell structure [171]. The SiO_2 shell not only provides excellent electrolyte wettability but also significantly enhances the tensile strength and thermal stability of the separator. Self-extinguishing separators considerably improve the safety of NCM811 batteries. As illustrated in Figure 21c, Wang et al. developed a freestanding separator based on a fluorinated COF [172]. This separator exhibits outstanding thermal stability and self-extinguishing properties. During combustion, the released HF gas suppresses radical chain reactions, effectively mitigating the thermal runaway risk of NCM811 batteries.

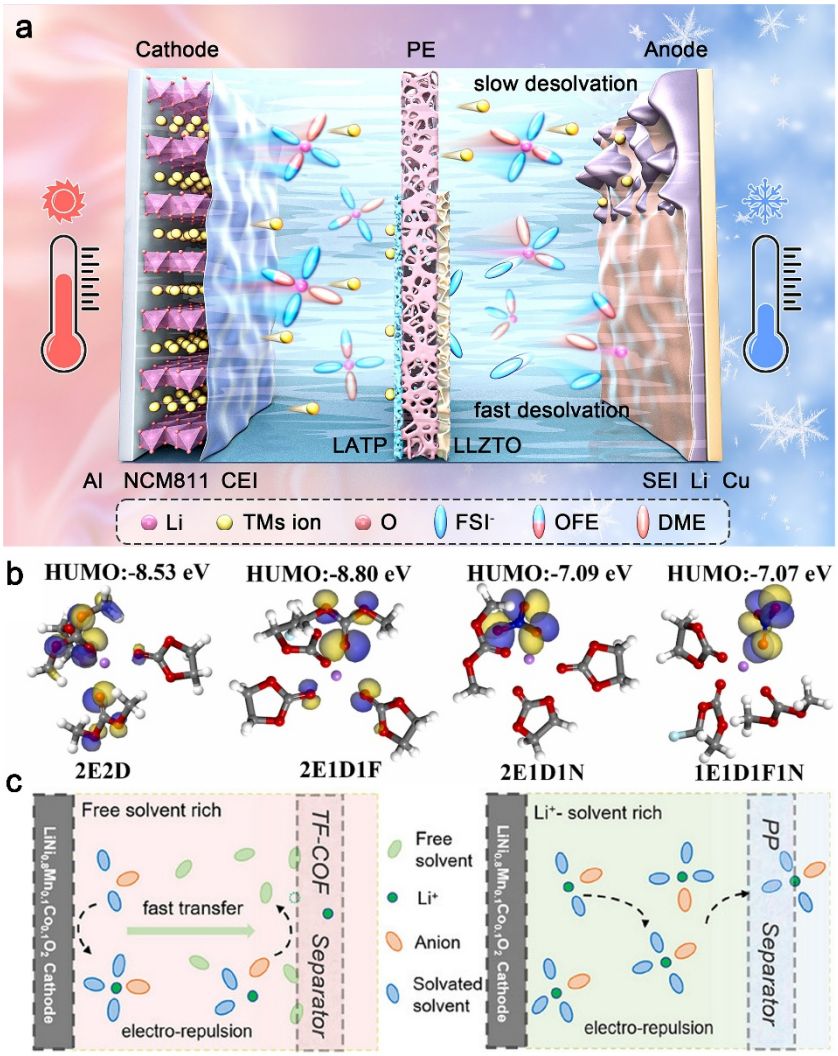


Figure 20. (**a**) Functional design strategy of SWS @ PE separator [166]. Copyright 2025, Elsevier B.V. (**b**) Representative solvated structures of the HOMO obtained from DFT calculations [168]. Copyright 2025, Elsevier B.V. (**c**) Schematic illustration of the electrolyte solvation configuration at the NCM811/electrolyte interface with TF-COF and PP separator [172]. Copyright 2025, Wiley-VCH.

3.5.2. Solid-State Electrolyte

The failure of NCM811 in liquid electrolytes is mainly caused by side reactions at the solid-liquid interface. Solid-state electrolytes (SSEs) offer a highly promising solution to this problem by completely removing organic solvent molecules, thereby addressing the inherent instability of NCM811.

Under high voltage, the highly reactive Ni^{4+} on the NCM811 surface accelerates the breakdown of liquid organic solvents. This process often leads to the release of lattice oxygen, forming an irreversible rock-salt layer on the surface and releasing oxygen gas. In contrast, SSEs can effectively prevent this irreversible oxygen release due to their superior stability under high voltage. Xu et al. developed a stable covalent organic framework (COF) SSE with well-aligned ion transport channels [173]. By adding quinoline rings and electron-withdrawing groups to the material, they increased the decomposition of electrolyte voltage to 5.6 V, creating an inherently stable interface. SSEs also effectively reduce side reactions and prevent the dissolution of TM ions. Even if some TM ions dissolve from the NCM811 surface, they cannot pass through the dense SSE layer to reach the negative electrode. As shown in Figure 21a, Wang et al. introduced strongly electron-withdrawing Mg^{2+} and Al^{3+} into a PEO-based electrolyte, which changed the electron distribution and coordination environment of the polymer chains [174]. This modification significantly improved the ability of electrolyte to resist oxidation and remain stable at high voltages. The interaction between these metal ions and the polymer chains reduced electron density, weakening their reaction with highly oxidized Ni^{4+} and thus reducing side reactions and nickel dissolution. Furthermore, this interaction helped form a stable protective layer on the cathode surface, rich in inorganic compounds like LiF, MgF_2, and AlF_3, which effectively protects the NCM811 interface. Additionally, SSEs with high stiffness can physically restrain the expansion and contraction of NCM811 particles. This helps reduce

internal stress and slows down the formation and growth of microcracks. As shown in Figure 21b, Zhao et al. created an SSE with both high stiffness and good stress-absorption properties using arrays of amorphous ceramic nanotubes [175]. This electrolyte effectively buffers mechanical stress and can accommodate the uneven volume changes of NCM811 particles during cycling. Moreover, in their review, Eckert and Rodrigues proposed that NASICON-type glass-ceramics can be used as solid electrolytes, combining high ionic conductivity with favorable interfacial properties, and that optimizing material composition and interface stability also serves as an effective strategy for performance enhancement [176].

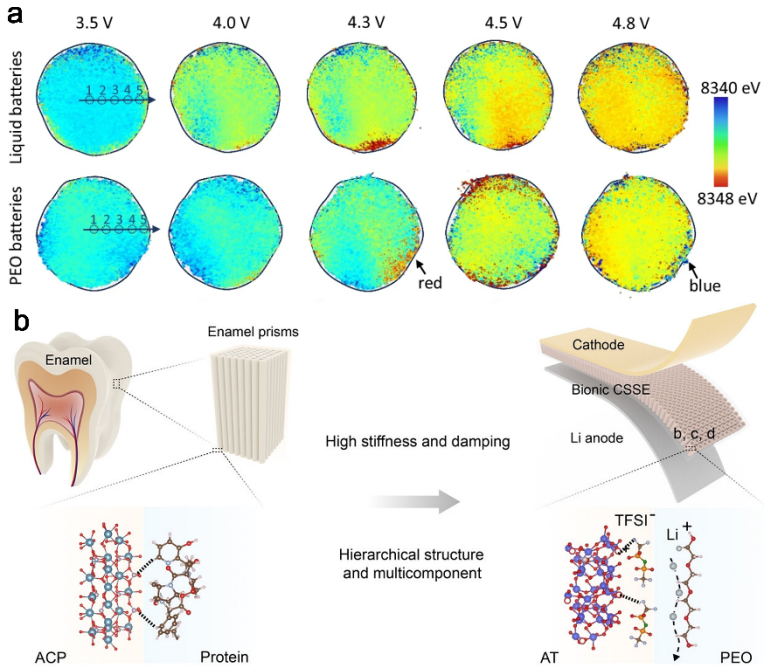


Figure 21. (**a**) Transmission X-ray microscopy images of cathode particles with different charge states in PEO-based solid and liquid electrolytes [174]. Copyright 2024, Springer Nature. (**b**) The hierarchical structure of enamel has been mimicked in the design of CSSE, allowing it to resist external impacts and maintain mechanical compatibility with electrodes [175]. Copyright 2025, Wiley-VCH.

However, the interface between the NCM811 cathode and SSEs still faces significant challenges: (1) Poor physical contact at the CEI, leading to increased resistance and degraded electrochemical performance; (2) Interfacial side reactions due to their oxidative characteristics, particularly the spontaneous chemical reactions that may occur when Ni-rich layered cathodes contact sulfide-based SSEs, resulting from their chemical potential mismatch; (3) The space-charge layer formed at the interface due to the potential difference, which significantly increases interfacial resistance and polarization.

4. Summary and Perspectives

NCM811 has attracted wide attention owing to its advantages such as high capacity and good rate capability. However, its large-scale application is seriously limited by structural degradation and interfacial side reactions. This article thoroughly discusses the degradation mechanisms of NCM811, including side reactions caused by residual lithium compounds, dissolution of transition metals, lattice oxygen release at high voltage, cation mixing, harmful phase transitions, microcrack propagation, and thermal runaway risks. In response to these issues, researchers have proposed various strategies, including bulk doping, synthesis of single-crystal particles, microstructure design, coating protection, and concentration gradient structures to enhance the structural and interfacial stability of NCM811. Rational design of key components (electrolyte, separator, solid electrolyte) in Ni-rich batteries promotes the formation of a stable electrode-electrolyte interface and the scavenging of HF, leading to improved long-cycle stability of the NCM811 cathode. Table 1 systematically reviews and compares the reported electrochemical performance improvement of high nickel cathodes achieved by different strategies. Nevertheless, each strategy has its own limitations, and no single method can comprehensively address all the challenges.

Table 1. Inhibition strategy and their electrochemical properties.

Inhibition Strategy	Materials	Loading ($mg \cdot cm^{-2}$)	C Rate	Initial Capacity ($mAh \cdot g^{-1}$)	Final Capacity ($mAh \cdot g^{-1}$)/Cycle Numbers	Capacity Retention/Decay Rate (%)	Reference
Cationic doping	W and Nb doping	3–4	10	148.5	77.7/500	52.3	[88]
Anionic doping	P-doped	2	1	221.9	182.2/300	82.1	[97]
Multi-ion co-doping	PO_4^{3-} and Mn^{4+}	3.5 ± 0.2	5	157.8	134.1/250	85	[102]
Synthesis of single crystal	single-crystal	2–3	1	173.6	163/100	93.9	[108]
Microstructural engineering	petal-grained $Li[Ni_{0.89}Co_{0.10}Sb_{0.01}]O_2$	5	0.5	217.9	207/100	95	[115]
Functional design of coating materials	Se-doped and $FeSe_2$&Fe_2O_3	14	1	225.8	180/500	79.7	[135]
Coating processes	Amorphous Li_3PO_4 layer	2	1	189.9	136/100	71.6	[144]
Functional additives	N,N-dimethyl-4-(4,4,5,5-tetramethyl-1,3,2-dioxaborolan-2-yl) aniline	3.54	1	163.1	145/140	88.9	[148]
Localized high-concentration electrolyte	1.2 m lithium bis(fluorosulfonyl)imide in a mixture of dimethyl carbonate/bis(2,2,2-trifluoroethyl) ether (1:2 by mol)	2	1	150	142.5/300	95	[153]
Novel solvent and lithium salt	4-methyl-1,3-dioxolane (MDOL) and 4-(trifluoromethyl)-1,3-dioxolane	8	1	165.2	147/100	89	[159]
Functionalized separator	PI/PVDF	3.24	1	~160	-/400	90.6	[161]
Solid-state electrolyte	covalent organic frameworks	2	1	~160	-/400	82	[174]

The various degradation mechanisms in NCM811 are intricate, intertwined and mutually reinforcing. First, a fundamental contradiction exists between bulk structure and interfacial stability. For example, inert coatings applied to suppress surface side reactions often concurrently impede lithium-ion transport across interfaces, resulting in degraded kinetic performance. This issue is particularly pronounced in all-solid-state battery systems. Second, atomic-level insights into the dynamic structural evolution of materials during long-term cycling remain limited. The existing characterization techniques mainly focus on the static analysis of the initial and final states. However, there is still a lack of sufficient real-time observation and in-depth understanding of the key dynamic processes, such as the initiation and propagation of microcracks, the accumulation of local lattice phase transitions, and the migration and dissolution of transition metal ions. This limitation constrains the ability to predict and precisely regulate failure mechanisms. Finally, a significant gap persists in transitioning from laboratory research to large-scale production. Many modification strategies that exhibit excellent performance in laboratory settings, including precise gradient doping and uniform atomic-layer-thick coatings, face challenges in scalability due to complex processing requirements, elevated costs, and stringent operational conditions. Therefore, future research should address the above core challenges to be solved and shift towards an "atom-to-system" holistic design.

(1) The synergistic effects achieved by integrating multiple strategies are crucial for suppressing both structural degradation and interfacial side reactions in NCM811. For instance, constructing a concentration-gradient structure using single-crystal particles with functional coatings is a promising approach to achieve comprehensive stabilization, spanning from the atomic scale to the macro-interface.
(2) Guided by dynamic insights from advanced in situ/operando characterization techniques (e.g., XANES, HR-STEM, HAADF-STEM), a deeper understanding of the real-time evolution of the structure and interface of the NCM811 cathode during cycling can be achieved.
(3) Designing electrolytes and functional separators that incorporate flame-retardant properties and scavenging capabilities for harmful substances is essential for enhancing battery safety. The gradual transition toward all-solid-state batteries represents a clear strategic direction. However, challenges in interfacial compatibility and Li^+ transport kinetics must be overcome.
(4) The further development of scalable, cost-effective, and environmentally benign synthesis and modification processes is imperative to bridge the gap between laboratory innovation and large-scale industrial application.

To realize the full potential of NCM811, advancements in material design must be coupled with optimized electrode engineering and scalable manufacturing. The choice of electrode parameters, such as thickness, areal

loading, and particle morphology-critically influences rate capability, mechanical integrity, and long-term cyclability. Manufacturing processes, including slurry coating and calendering, determine the electrode's microstructure, which directly affects ionic/electronic conductivity and interfacial stability. Surface and interface engineering must ensure durability under prolonged cycling stresses. Furthermore, the initial electrode architecture defines its aging trajectory, making the study of processing-structure-performance relationships under realistic conditions essential. A holistic approach integrating material synthesis, electrode design, and cell assembly is key to bridging lab-scale innovation with commercial application.

Notwithstanding the aforementioned challenges, rapid advances in characterization techniques, structural design, and modification strategies are poised to enable groundbreaking advances in the energy density, cycle life, and safety of NCM811 batteries.

Author Contributions: Y.H. (Yuhui He): conceptualization, writing—original draft preparation; H.X.: data curation, writing—original draft preparation; Y.H. (Yupei Han): data curation, Investigation, visualization; W.H.: conceptualization, supervision, Writing—review & editing. All authors have read and agreed to the published version of the manuscript.

Funding: This research was funded by Chongqing Technology Innovation and Application Development Special Key Project, grant number CSTB2023TIAD-KPX0010 and Chongqing Technology Innovation and Application Development Special Major Project, grant number CSTB2023TIAD-STX0033, and Natural Science Foundation of Chongqing, China, grant number CSTB2022NSCQ-MSX0246, CSTB2022NSCQ-MSX1572, and the Science Foundation of National Key Laboratory of Science and Technology on Advanced Composites in Special Environments.

Institutional Review Board Statement: Not applicable.

Informed Consent Statement: Not applicable.

Data Availability Statement: No new data was generated for this review. All data presented, including those summarized in tables and figures, are based on previously published studies.

Conflicts of Interest: Given the role as Editor-in-Chief, Weidong He had no involvement in the peer review of this paper and had no access to information regarding its peer-review process. Full responsibility for the editorial process of this paper was delegated to another editor of the journal.

Use of AI and AI-Assisted Technologies: No AI tools were utilized for this paper.

References

1. Yin, Y.C.; Yang, J.T.; Luo, J.D.; et al. A $LaCl_3$-Based Lithium Superionic Conductor Compatible with Lithium Metal. *Nature* **2023**, *616*, 77–83.
2. Zhou, L.; Zuo, T.-T.; Kwok, C.Y.; et al. High Areal Capacity, Long Cycle Life 4 V Ceramic All-Solid-State Li-Ion Batteries Enabled by Chloride Solid Electrolytes. *Nat. Energy* **2022**, *7*, 83–93.
3. Kim, U.-H.; Park, G.-T.; Son, B.-K.; et al. Heuristic Solution for Achieving Long-Term Cycle Stability for Ni-Rich Layered Cathodes at Full Depth of Discharge. *Nat. Energy* **2020**, *5*, 860–869.
4. Li, W.; Erickson, E.M.; Manthiram, A. High-Nickel Layered Oxide Cathodes for Lithium-Based Automotive Batteries. *Nat. Energy* **2020**, *5*, 26–34.
5. Liu, W.; Oh, P.; Liu, X.; et al. Nickel-Rich Layered Lithium Transition-Metal Oxide for High-Energy Lithium-Ion Batteries. *Angew. Chem. Int. Ed.* **2015**, *54*, 4440–4457.
6. Myung, S.-T.; Maglia, F.; Park, K.-J.; et al. Nickel-Rich Layered Cathode Materials for Automotive Lithium-Ion Batteries: Achievements and Perspectives. *ACS Energy Lett.* **2016**, *2*, 196–223.
7. Yoon, M.; Dong, Y.; Hwang, J.; et al. Reactive Boride Infusion Stabilizes Ni-Rich Cathodes for Lithium-Ion Batteries. *Nat. Energy* **2021**, *6*, 362–371.
8. Li, W.; Asl, H.Y.; Xie, Q.; et al. Collapse of $LiNi_{1-x-y}Co_xMn_yO_2$ Lattice at Deep Charge Irrespective of Nickel Content in Lithium-Ion Batteries. *J. Am. Chem. Soc.* **2019**, *141*, 5097–5101.
9. Liu, J.; Bao, Z.; Cui, Y.; et al. Pathways for Practical High-Energy Long-Cycling Lithium Metal Batteries. *Nat. Energy* **2019**, *4*, 180–186.
10. Manthiram, A. A Reflection on Lithium-Ion Battery Cathode Chemistry. *Nat. Commun.* **2020**, *11*, 1550.
11. Hu, J.; Li, L.; Bi, Y.; et al. Locking Oxygen in Lattice: A Quantifiable Comparison of Gas Generation in Polycrystalline and Single Crystal Ni-Rich Cathodes. *Energy Storage Mater.* **2022**, *47*, 195–202.
12. Teichert, P.; Jahnke, H.; Figgemeier, E. Degradation Mechanism of Monocrystalline Ni-Rich $Li[Ni_xMn_yCo_z]O_2$ (NMC) Active Material in Lithium Ion Batteries. *J. Electrochem. Soc.* **2021**, *168*, 090532.
13. Hu, J.; Li, L.; Hu, E.; et al. Mesoscale-Architecture-Based Crack Evolution Dictating Cycling Stability of Advanced Lithium Ion Batteries. *Nano Energy* **2021**, *79*, 105420.
14. Ryu, H.-H.; Namkoong, B.; Kim, J.-H.; et al. Capacity Fading Mechanisms in Ni-Rich Single-Crystal NCM Cathodes. *ACS Energy Lett.* **2021**, *6*, 2726–2734.

15. Lin, Q.; Guan, W.; Zhou, J.; et al. Ni-Li Anti-Site Defect Induced Intragranular Cracking in Ni-Rich Layer-Structured Cathode. *Nano Energy* **2020**, *76*, 105021.
16. Li, S.; Yao, Z.; Zheng, J.; et al. Direct Observation of Defect-Aided Structural Evolution in a Nickel-Rich Layered Cathode. *Angew. Chem. Int. Ed.* **2020**, *59*, 22092–22099.
17. Britala, L.; Marinaro, M.; Kucinskis, G. A Review of the Degradation Mechanisms of NCM Cathodes and Corresponding Mitigation Strategies. *J. Energy Storage* **2023**, *73*, 108875.
18. Maleki Kheimeh Sari, H.; Li, X. Controllable Cathode–Electrolyte Interface of $Li[Ni_{0.8}Co_{0.1}Mn_{0.1}]O_2$ for Lithium Ion Batteries: A Review. *Adv. Energy Mater.* **2019**, *9*, 1901597.
19. Zheng, Y.; Li, J.; Liu, Y.; et al. Challenges and Advancements in High-Nickel Layered Oxides Cathode Material for Lithium-Ion Batteries. *Energy Environ. Mater.* **2025**, e70152. https://doi.org/10.1002/eem2.70152.
20. Renfrew, S.E.; McCloskey, B.D. Residual Lithium Carbonate Predominantly Accounts for First Cycle CO_2 and CO Outgassing of Li-Stoichiometric and Li-Rich Layered Transition-Metal Oxides. *J. Am. Chem. Soc.* **2017**, *139*, 17853–17860.
21. Zhang, Y.; Katayama, Y.; Tatara, R.; et al. Revealing Electrolyte Oxidation via Carbonate Dehydrogenation on Ni-Based Oxides in Li-Ion Batteries by In Situ Fourier Transform Infrared Spectroscopy. *Energy Environ. Sci.* **2020**, *13*, 183–199.
22. Kim, Y.; Park, H.; Warner, J.H.; et al. Unraveling the Intricacies of Residual Lithium in High-Ni Cathodes for Lithium-Ion Batteries. *ACS Energy Lett.* **2021**, *6*, 941–948.
23. Chen, G.; Yang, H.; Liu, L.; et al. Conversion of Residual Lithium into Fast Lithium Ion Conductor Coating to Achieve High Cycle Life $LiNi_{0.8}Co_{0.15}Al_{0.05}O_2$ Cathode for Lithium Ion Battery. *J. Mater. Sci. Mater. Electron.* **2024**, *35*, 280.
24. Karger, L.; Yao, R.; Seidel, K.; et al. Solving the Residual Lithium Problem by Substoichiometric Synthesis of Layered Ni-Rich Oxide Cathodes. A*CS Energy Lett.* **2024**, *9*, 5573–5575.
25. Huang, T.Y.; Cai, Z.; Crafton, M.J.; et al. Chemical Origin of In Situ Carbon Dioxide Outgassing from a Cation-Disordered Rock Salt Cathode. *Chem. Mater.* **2024**, *36*, 6535–6546.
26. Kaufman, L.A.; McCloskey, B.D. Surface Lithium Carbonate Influences Electrolyte Degradation via Reactive Oxygen Attack in Lithium-Excess Cathode Materials. *Chem. Mater.* **2021**, *33*, 4170–4176.
27. Fang, Z.; Confer, M.P.; Wang, Y.; et al. Formation of Surface Impurities on Lithium-Nickel-Manganese-Cobalt Oxides in the Presence of CO_2 and H_2O. *J. Am. Chem. Soc.* **2021**, *143*, 10261–10274.
28. Chen, Z.; Li, J.; Zeng, X.C. Unraveling Oxygen Evolution in Li-Rich Oxides: A Unified Modeling of the Intermediate Peroxo/Superoxo-like Dimers. *J. Am. Chem. Soc.* **2019**, *141*, 10751–10759.
29. Teufl, T.; Strehle, B.; Müller, P.; et al. Oxygen Release and Surface Degradation of Li- and Mn-Rich Layered Oxides in Variation of the Li_2MnO_3 Content. *J. Electrochem. Soc.* **2018**, *165*, A2718–A2731.
30. Eum, D.; Kim, B.; Kim, S.J.; et al. Voltage Decay and Redox Asymmetry Mitigation by Reversible Cation Migration in Lithium-Rich Layered Oxide Electrodes. *Nat. Mater.* **2020**, *19*, 419–427.
31. Strehle, B.; Kleiner, K.; Jung, R.; et al. The Role of Oxygen Release from Li- and Mn-Rich Layered Oxides during the First Cycles Investigated by On-Line Electrochemical Mass Spectrometry. *J. Electrochem. Soc.* **2017**, *164*, A400–A406.
32. Hong, J.; Gent, W.E.; Xiao, P.; et al. Metal-Oxygen Decoordination Stabilizes Anion Redox in Li-Rich Oxides. *Nat. Mater.* **2019**, *18*, 256–265.
33. Sathiya, M.; Abakumov, A.M.; Foix, D.; et al. Origin of Voltage Decay in High-Capacity Layered Oxide Electrodes. *Nat. Mater.* **2015**, *14*, 230–238.
34. Zheng, C.; Wang, Y.; Mao, H.; et al. Superexchange Interaction Regulates Ni/Mn Spin States Triggering Ni-t_{2g}/O-2p Reductive Coupling Enabling Stable Lithium-Rich Cathode. *Nat. Commun.* **2025**, *16*, 3900.
35. Hu, E.; Yu, X.; Lin, R.; et al. Evolution of Redox Couples in Li- and Mn-Rich Cathode Materials and Mitigation of Voltage Fade by Reducing Oxygen Release. *Nat. Energy* **2018**, *3*, 690–698.
36. Yu, H.L.; Ibrahim, K.B.; Chi, P.W.; et al. Modulating the Voltage Decay and Cationic Redox Kinetics of Li-Rich Cathodes via Controlling the Local Electronic Structure. *Adv. Funct. Mater.* **2022**, *32*, 2112394.
37. Liu, T.; Dai, A.; Lu, J.; et al. Correlation between Manganese Dissolution and Dynamic Phase Stability in Spinel-Based Lithium-Ion Battery. *Nat. Commun.* **2019**, *10*, 4721.
38. Gent, W.E.; Lim, K.; Liang, Y.; et al. Coupling between Oxygen Redox and Cation Migration Explains Unusual Electrochemistry in Lithium-Rich Layered Oxides. *Nat. Commun.* **2017**, *8*, 2091.
39. Zhan, C.; Wu, T.; Lu, J.; et al. Dissolution, Migration, and Deposition of Transition Metal Ions in Li-Ion Batteries Exemplified by Mn-Based Cathodes-a Critical Review. *Energy Environ. Sci.* **2018**, *11*, 243–257.
40. McColl, K.; House, R.A.; Rees, G.J.; et al. Transition Metal Migration and O_2 Formation Underpin Voltage Hysteresis in Oxygen-Redox Disordered Rock Salt Cathodes. *Nat. Commun.* **2022**, *13*, 5275.
41. Zheng, J.; Ye, Y.; Liu, T.; et al. Ni/Li Disordering in Layered Transition Metal Oxide: Electrochemical Impact, Origin, and Control. *Acc. Chem. Res.* **2019**, *52*, 2201–2209.
42. Qian, G.; Zhang, J.; Chu, S.-Q.; et al. Understanding the Mesoscale Degradation in Nickel-Rich Cathode Materials through Machine-Learning-Revealed Strain-Redox Decoupling. *ACS Energy Lett.* **2021**, *6*, 687–693.

43. Zhang, X.; Zhao, W.; Li, R.; et al. Moisture-Scavenging Electrolyte for High-Temperature Stable Lithium-Ion Batteries. *Energy Storage Mater.* **2025**, *80*, 104409.
44. Gan, Q.; Qin, N.; Li, Z.; et al. Surface Spinel Reconstruction to Suppress Detrimental Phase Transition for Stable $LiNi_{0.8}Co_{0.1}Mn_{0.1}O_2$ Cathodes. *Nano Res.* **2022**, *16*, 513–520.
45. Cheng, X.; Liu, X.; Zhao, L.; et al. Pre-Deoxidation of Layered Ni-Rich Cathodes to Construct a Stable Interface with Electrolyte for Long Cycling Life. *Adv. Funct. Mater.* **2022**, *33*, 2211171.
46. Zheng, C.; Zhang, J.; Mao, H.; et al. Entropic Design of Anionic Site to Improve Anionic Redox Stability in Lithium-Rich Cathode. *Adv. Mater.* **2024**, *36*, e2413785.
47. Tan, X.; Chen, Z.; Liu, T.; et al. Imitating Architectural Mortise-Tenon Structure for Stable Ni-Rich Layered Cathodes. *Adv. Mater.* **2023**, *35*, e2301096.
48. Huang, Q.; Zhang, X.; Lv, X.; et al. Electrochemical Aging Protocol Governed Capacity Losses and Structure Degradations in Layered $LiNi_{0.8}Co_{0.1}Mn_{0.1}O_2$ Oxides. *Small* **2023**, *19*, 2302086.
49. Yuan, Q.; Zhao, F.; Wang, W.; et al. Overcharge Failure Investigation of Lithium-Ion Batteries. *Electrochim. Acta* **2015**, *178*, 682–688.
50. Xu, C.; Reeves, P.J.; Jacquet, Q.; et al. Phase Behavior during Electrochemical Cycling of Ni-Rich Cathode Materials for Li-Ion Batteries. *Adv. Energy Mater.* **2020**, *11*, 2003404.
51. Wang, L.; Su, Q.; Han, B.; et al. Unraveling the Degradation Mechanism of $LiNi_{0.8}Co_{0.1}Mn_{0.1}O_2$ at the High Cut-Off Voltage for Lithium Ion Batteries. *J. Energy Chem.* **2023**, *77*, 428–437.
52. Xu, J.; Hu, E.; Nordlund, D.; et al. Understanding the Degradation Mechanism of Lithium Nickel Oxide Cathodes for Li-Ion Batteries. *ACS Appl. Mater. Interfaces* **2016**, *8*, 31677–31683.
53. Liang, C.; Jiang, L.; Wei, Z.; et al. Insight into the Structural Evolution and Thermal Behavior of $LiNi_{0.8}Co_{0.1}Mn_{0.1}O_2$ Cathode under Deep Charge. *J. Energy Chem.* **2022**, *65*, 424–432.
54. Wu, F.; Liu, N.; Chen, L.; et al. Improving the Reversibility of the H2–H3 Phase Transitions for Layered Ni-Rich Oxide Cathode towards Retarded Structural Transition and Enhanced Cycle Stability. *Nano Energy* **2019**, *59*, 50–57.
55. Wu, F.; Liu, N.; Chen, L.; et al. The Nature of Irreversible Phase Transformation Propagation in Nickel-Rich Layered Cathode for Lithium-Ion Batteries. *J. Energy Chem.* **2021**, *62*, 351–358.
56. Han, G.-M.; Kim, Y.-S.; Ryu, H.-H.; et al. Structural Stability of Single-Crystalline Ni-Rich Layered Cathode upon Delithiation. *ACS Energy Lett.* **2022**, *7*, 2919–2926.
57. Kondrakov, A.O.; Schmidt, A.; Xu, J.; et al. Anisotropic Lattice Strain and Mechanical Degradation of High- and Low-Nickel NCM Cathode Materials for Li-Ion Batteries. *J. Phys. Chem. C* **2017**, *121*, 3286–3294.
58. Ryu, H.-H.; Park, N.-Y.; Noh, T.-C.; et al. Microstrain Alleviation in High-Energy Ni-Rich NCMA Cathode for Long Battery Life. *ACS Energy Lett.* **2020**, *6*, 216–223.
59. Lee, W.; Choi, M.; Kim, M.; et al. Pinning Effects of Heavy Elements for the Structural Stability of Ni-Based Layered Oxides. *ACS Energy Lett.* **2025**, *10*, 4527–4534.
60. Zheng, S.; Hong, C.; Guan, X.; et al. Correlation between Long Range and Local Structural Changes in Ni-Rich Layered Materials During Charge and Discharge Process. *J. Power Sources* **2019**, *412*, 336–343.
61. Tang, J.; Zhao, B.; Wang, Z.; et al. Atomic-Resolution In Situ Exploration of the Phase Transition Triggered Failure in a Single-Crystalline Ni-Rich Cathode. *ACS Appl. Mater. Interfaces* **2024**, *16*, 16075–16085.
62. Shishvan, S.S.; Fleck, N.A.; McMeeking, R.M.; et al. Cracking and Associated Volumetric Expansion of NMC811 Secondary Particles. *J. Power Sources* **2023**, *588*, 233745.
63. Pegel, H.; von Kessel, O.; Heugel, P.; et al. Volume and Thickness Change of NMC811|SiO_x-Graphite Large-Format Lithium-Ion Cells: From Pouch Cell to Active Material Level. *J. Power Sources* **2022**, *537*, 231443.
64. Ma, H.; Cai, S.; Song, R.; et al. Evolution of Interfacial Electro-Chemo-Mechanics in High-Energy-Density NCM811||Si/C-Composite Lithium-Ion Pouch Cells. *Chem. Eng. J.* **2025**, *511*, 162081.
65. Wang, X.; Song, Y.; Cui, H.; et al. Insight into the Electrochemical Behaviors of NCM811|SiO-Gr Pouch Battery through Thickness Variation. *Energy Environ. Mater.* **2023**, *6*, e12401.
66. Park, K.-J.; Hwang, J.-Y.; Ryu, H.-H.; et al. Degradation Mechanism of Ni-Enriched NCA Cathode for Lithium Batteries: Are Microcracks Really Critical? *ACS Energy Lett.* **2019**, *4*, 1394–1400.
67. Lim, J.M.; Hwang, T.; Kim, D.; et al. Intrinsic Origins of Crack Generation in Ni-Rich $LiNi_{0.8}Co_{0.1}Mn_{0.1}O_2$ Layered Oxide Cathode Material. *Sci. Rep.* **2017**, *7*, 39669.
68. Heenan, T.M.M.; Wade, A.; Tan, C.; et al. Identifying the Origins of Microstructural Defects Such as Cracking within Ni-Rich NMC811 Cathode Particles for Lithium-Ion Batteries. *Adv. Energy Mater.* **2020**, *10*, 2002655.
69. Shen, W.; Li, K.; Huang, J.; et al. Core-Shell NCM Cathode Particles Mechanical Failure: Particle Cracking and Interfacial Debonding. *ACS Appl. Energy Mater.* **2024**, *7*, 6384–6399.
70. Nam, G.W.; Park, N.-Y.; Park, K.-J.; et al. Capacity Fading of Ni-Rich NCA Cathodes: Effect of Microcracking Extent. *ACS Energy Lett.* **2019**, *4*, 2995–3001.

71. Park, N.-Y.; Park, G.-T.; Kim, S.-B.; et al. Degradation Mechanism of Ni-Rich Cathode Materials: Focusing on Particle Interior. *ACS Energy Lett.* **2022**, *7*, 2362–2369.
72. Meng, X.H.; Lin, T.; Mao, H.; et al. Kinetic Origin of Planar Gliding in Single-Crystalline Ni-Rich Cathodes. *J. Am. Chem. Soc.* **2022**, *144*, 11338–11347.
73. Wei, Z.; Fang, Z.; Liang, C.; et al. Deciphering the Synergistic Mechanism for Thermal Stability Improvement in Ni-Rich Single-Crystal Cathode Materials via $LiNbO_3$ Coating and Nb^{5+} Surface Doping. *Innov. Energy* **2025**, *2*, 100083.
74. Wu, Y.; Zhang, W.; Rui, X.; et al. Thermal Runaway Mechanism of Composite Cathodes for All-Solid-State Batteries. *Adv. Energy Mater.* **2025**, *15*, 2405183.
75. Cui, Z.; Manthiram, A. Thermal Stability and Outgassing Behaviors of High-Nickel Cathodes in Lithium-Ion Batteries. *Angew. Chem. Int. Ed.* **2023**, *62*, e202307243.
76. Wang, Y.; Feng, X.; Huang, W.; et al. Challenges and Opportunities to Mitigate the Catastrophic Thermal Runaway of High-Energy Batteries. *Adv. Energy Mater.* **2023**, *13*, 2203841.
77. Lee, E.; Muhammad, S.; Kim, T.; et al. Tracking the Influence of Thermal Expansion and Oxygen Vacancies on the Thermal Stability of Ni-Rich Layered Cathode Materials. *Adv. Sci.* **2020**, *7*, 1902413.
78. Zhou, G.; Liu, Y.; Li, Y.; et al. Experimental Study on the Thermal Runaway Acceleration Mechanism and Characteristics of NCM811 Lithium-Ion Battery with Critical Thermal Load Induced by Nail Penetration. *J. Clean. Prod.* **2024**, *434*, 140121.
79. Shin, Y.; Ahn, K.; Lee, C.; et al. A Self-Discharging Reaction Mediated by Imide Salt Enables the Prevention of Explosive Thermal Runaway in High-Ni Material/Graphite Full Cells. *J. Mater. Chem. A Mater.* **2023**, *11*, 23556–23565.
80. Lu, Z.; Liu, D.; Dai, K.; et al. Tailoring Solvation Chemistry in Carbonate Electrolytes for All-Climate, High-Voltage Lithium-Rich Batteries. *Energy Storage Mater.* **2023**, *57*, 316–325.
81. Wang, Y.; Ren, D.; Feng, X.; et al. Thermal runaway Modeling of large Format High-Nickel/Silicon-Graphite Lithium-Ion Batteries Based on Reaction Sequence and Kinetics. *Appl. Energy* **2022**, *306*, 117943.
82. Huang, Y.; Xu, Y.; Zhang, P.; et al. In-Depth Study of Gas-Solid Jet and Formation Mechanisms During Thermal Runaway in Ternary Lithium-Ion Batteries. *Energy* **2025**, *324*, 135982.
83. Li, H.; Shen, H.; Li, M.; et al. A Simplified Mathematical Modeling Approach for Thermal Runaway of $LiNi_{0.8}Co_{0.1}Mn_{0.1}O_2$ Pouch Cells Based on Thermal Runaway Experimental Data. *J. Energy Storage* **2024**, *90*, 111829.
84. Lu, J.; Yan, C.; Min, X.; et al. Nb/Al Codoping Strategy for Nickel-Rich Cathodes to Improve Rate and Cycle Performance of Lithium-Ion Batteries. *Energy Fuels* **2025**, *39*, 7057–7068.
85. Zheng, J.; Zhao, S.; Guan, W.; et al. Tungsten-Doping Enables Excellent Kinetics and High Stability of Cobalt-Free Ultrahigh-Nickel Single-Crystal Cathode. *Energy Storage Mater.* **2025**, *78*, 104251.
86. Park, N.Y.; Cho, G.; Kim, S.B.; et al. Multifunctional Doping Strategy to Develop High-Performance Ni-Rich Cathode Material. *Adv. Energy Mater.* **2023**, *13*, 2204291.
87. Weigel, T.; Schipper, F.; Erickson, E.M.; et al. Structural and Electrochemical Aspects of $LiNi_{0.8}Co_{0.1}Mn_{0.1}O_2$ Cathode Materials Doped by Various Cations. *ACS Energy Lett.* **2019**, *4*, 508–516.
88. Yang, R.; Xie, J.; Li, J.; et al. Synergistic Modification and Mechanism of Tungsten and Niobium to Enhance the Performance of Nickel-Rich Layered Cathode Materials. *Small* **2025**, *21*, e2409426.
89. Wang, W.; Zhou, Y.; Zhang, B.; et al. Optimized In Situ Doping Strategy Stabling Single-Crystal Ultrahigh-Nickel Layered Cathode Materials. *ACS Nano* **2024**, *18*, 8002–8016.
90. Ou, X.; Liu, T.; Zhong, W.; et al. Enabling High Energy Lithium Metal Batteries via Single-Crystal Ni-Rich Cathode Material Co-Doping Strategy. *Nat. Commun.* **2022**, *13*, 2319.
91. Lee, S.-B.; Park, N.-Y.; Park, G.-T.; et al. Doping Strategy in Developing Ni-Rich Cathodes for High-Performance Lithium-Ion Batteries. *ACS Energy Lett.* **2024**, *9*, 740–747.
92. Liao, H.; Tang, Y.; Ma, W.; et al. Exceptional Layered Cathode Stability at 4.8 V via Supersaturated High-Valence Cation Design. *Nat. Energy* **2025**, *10*, 1107–1115.
93. Chakraborty, A.; Bano, A.; Kunnikuruvan, S.; et al. Doping Strategies in Ni-Rich NCM Cathode Materials for Next-Generation Li-Ion Batteries: A Systematic Computational Study. *ACS Appl. Energy Mater.* **2025**, *8*, 10445–10457.
94. Cao, B.; Fang, H.T.; Li, D.; et al. Single-Crystalline $LiNi_{0.8}Co_{0.1}Mn_{0.1}O_2$ Stabilized by F-Doping-Induced Superlattice for 4.8 V lithium-Ion Batteries. *Chem. Eng. J.* **2024**, *496*, 153821.
95. Li, F.; Liu, Z.; Liao, C.; et al. Gradient Boracic Polyanion Doping-Derived Surface Lattice Modulation of High-Voltage Ni-Rich Layered Cathodes for High-Energy-Density Li-Ion Batteries. *ACS Energy Lett.* **2023**, *8*, 4903–4914.
96. Yang, J.; Mao, G.; Yao, T.; et al. Fluorination from Surface to Bulk Stabilizing High Nickel Cathode Materials with Outstanding Electrochemical Performance. *Angew. Chem. Int. Ed.* **2025**, *64*, e202420413.
97. Lou, Y.; Lin, Z.; Shen, J.; et al. Simultaneous Regulating the Surface, Interface, and Bulk via Phosphating Modification for High-Performance Li-Rich Layered Oxides Cathodes. *Adv. Mater.* **2025**, *37*, e2416136.

98. Li, C.; Kan, W.H.; Xie, H.; et al. Inducing Favorable Cation Antisite by Doping Halogen in Ni-Rich Layered Cathode with Ultrahigh Stability. *Adv. Sci.* **2019**, *6*, 1801406.
99. Binder, J.O.; Culver, S.P.; Pinedo, R.; et al. Investigation of Fluorine and Nitrogen as Anionic Dopants in Nickel-Rich Cathode Materials for Lithium-Ion Batteries. *ACS Appl. Mater. Interfaces* **2018**, *10*, 44452–44462.
100. Yang, G.; Pan, K.; Lai, F.; et al. Integrated Co-Modification of PO_4^{3-} Polyanion Doping and Li_2TiO_3 Coating for Ni-Rich layered $LiNi_{0.6}Co_{0.2}Mn_{0.2}O_2$ Cathode material of Lithium-Ion Batteries. *Chem. Eng. J.* **2021**, *421*, 129964.
101. Zhang, Q.; Liu, K.; Li, C.; et al. The Surface Triple-Coupling on Single Crystalline Cathode for Lithium Ion Batteries. *Nano Energy* **2021**, *86*, 106096.
102. Qiu, L.; Xiang, W.; Tian, W.; et al. Polyanion and Cation Co-Doping Stabilized Ni-Rich Ni-Co-Al Material as Cathode with Enhanced Electrochemical Performance for Li-Ion Battery. *Nano Energy* **2019**, *63*, 103818.
103. Zhang, R.; Wang, C.; Zou, P.; et al. Compositionally Complex Doping for Zero-Strain Zero-Cobalt Layered Cathodes. *Nature* **2022**, *610*, 67–73.
104. Yang, B.; Zhou, L.; Hu, X.; et al. Enhancing the Electrochemical Performances of $LiNi_{0.8}Co_{0.15}Al_{0.05}O_2$ Cathode Material by Anion/Cation Co-Doping. *Ionics* **2021**, *27*, 1491–1499.
105. Shen, J.; Cao, Z.; Li, Z.; et al. Regulating Anion-Cation Band Centers to Inhibit Oxygen Escape and Phase Transition for Stable Single-Crystalline Ultrahigh-Ni Layered Cathodes. *Adv. Funct. Mater.* **2025**, *35*, 2502419.
106. Wei, Z.; Liang, C.; Jiang, L.; et al. Probing the Thermal Degradation Mechanism of Polycrystalline and Single-Crystal $LiNi_{0.8}Co_{0.1}Mn_{0.1}O_2$ Cathodes from the Perspective of Oxygen Vacancy Diffusion. *Energy Storage Mater.* **2023**, *56*, 495–505.
107. Heo, B.; Kim, M.; Hwang, C.; et al. Interfacial Stability Enhancement in Single-Crystal NCM Cathodes through Electronic Structure Optimization. *Mater. Today* **2025**, *90*, 322–333.
108. Zhou, H.; Ge, P.; Li, J.; et al. Homogenizing Phase-Component Regeneration of Spent NCM811 into Single-Crystal NCM622 with Enhanced Structural and Electrochemical Stability. *Energy Storage Mater.* **2025**, *82*, 104572.
109. Gao, H.; Yan, Q.; Tran, D.; et al. Upcycling of Spent $LiNi_{0.33}Co_{0.33}Mn_{0.33}O_2$ to Single-Crystal Ni-Rich Cathodes Using Lean Precursors. *ACS Energy Lett.* **2023**, *8*, 4136–4144.
110. Wang, Y.; Qiu, L.; Deng, Y.; et al. Facet-Stacking Coupling Accelerates Grain Growth During Synthesis of Single-Crystal Ni-Rich Cathodes. *Adv. Funct. Mater.* **2025**, e16097. https://doi.org/10.1002/adfm.202516097.
111. Kim, J.; Seo, J.-K.; Lee, B.-J.; et al. The Dual Role of Zirconium in Single-Crystal Ni-Rich Cathodes as a Promoter for Grain Growth and a Pillar for Structural Stability for High-Voltage Lithium-Ion Batteries. *Energy Storage Mater.* **2025**, *83*, 104718.
112. Zhang, T.; Qin, Z.; Long, X.; et al. Stable Molten Salts Mediated Growth of Single-Crystalline $LiNi_{0.8}Co_{0.1}Mn_{0.1}O_2$ with High Voltage Tolerance. *Adv. Funct. Mater.* **2025**, *35*, 2500608.
113. Li, J.; Li, H.; Stone, W.; et al. Synthesis of Single Crystal $LiNi_{0.5}Mn_{0.3}Co_{0.2}O_2$ for Lithium Ion Batteries. *J. Electrochem. Soc.* **2017**, *164*, A3529–A3537.
114. Wu, B.; Yi, R.; Xu, Y.; et al. Unusual Li_2O Sublimation Promotes Single-Crystal Growth and Sintering. *Nat. Energy* **2025**, *10*, 605–615.
115. Sun, H.H.; Dolocan, A.; Weeks, J.A.; et al. Stabilization of a Highly Ni-Rich Layered Oxide Cathode through Flower-Petal Grain Arrays. *ACS Nano* **2020**, *14*, 17142–17150.
116. Liu, T.; Yu, L.; Liu, J.; et al. Ultrastable Cathodes Enabled by Compositional and Structural Dual-Gradient Design. *Nat. Energy* **2024**, *9*, 1252–1263.
117. Wu, W.; Chen, S.; Wang, S.; et al. Micro-structure Regulation and Evolution of Hydroxide Precursor for Radially Aligned Ni-Rich Cathode with Superior Performance. *Chem. Eng. J.* **2025**, *512*, 162403.
118. Park, G.-T.; Park, N.-Y.; Noh, T.-C.; et al. High-Performance Ni-Rich $LiNi_{0.9-x}Co_{0.1}Al_xO_2$ Cathodes via Multi-Stage Microstructural Tailoring from Hydroxide Precursor to the Lithiated Oxide. *Energy Environ. Sci.* **2021**, *14*, 5084–5095.
119. Wang, S.; Zhou, X.; Zhao, T.; et al. Precise Regulation of Particle Orientation for Ni-Rich Cathodes with Ultra-Long Cycle Life. *Nano Energy* **2024**, *129*, 110008.
120. Wang, L.; Zhu, B.; Xiao, D.; et al. Grain Morphology and Microstructure Control in High-Stable Ni-Rich Layered Oxide Cathodes. *Adv. Funct. Mater.* **2023**, *33*, 2212849.
121. Park, N.-Y.; Han, S.-M.; Ryu, J.-H.; et al. Tailoring Primary Particle Size Distribution to Suppress Microcracks in Ni-Rich Cathodes via Controlled Grain Coarsening. *ACS Energy Lett.* **2024**, *9*, 3595–3604.
122. Guo, W.; Yu, H.; Wang, M.; et al. Compositional Gradient Design of Ni-Rich Co-Poor Cathodes Enhanced Cyclability and Safety in High-Voltage Li-Ion Batteries. *ACS Nano* **2025**, *19*, 8371–8380.
123. Park, G.-T.; Ryu, H.-H.; Noh, T.-C.; et al. Microstructure-Optimized Concentration-Gradient NCM Cathode for Long-Life Li-Ion Batteries. *Mater. Today* **2022**, *52*, 9–18.
124. Kim, S.; Thind, A.S.; Mohanty, S.K.; et al. High-Nickel Cathodes with Mechanical and Interfacial Robustness via Tailored Concentration Gradients for Stable Li-Ion Batteries. *ACS Energy Lett.* **2025**, *10*, 3600–3609.

125. Zheng, J.; Jiang, H.; Xu, X.; et al. In Situ Partial-Cyclized Polymerized Acrylonitrile-Coated NCM811 Cathode for High-Temperature ≥ 100 degrees C Stable Solid-State Lithium Metal Batteries. *Nano-Micro Lett.* **2025**, *17*, 195.
126. Xu, X.; Chu, S.; Xu, S.; et al. Integrating Prelithiation and Interface Protection to Achieve High-Energy All-Solid-State Batteries. *Angew. Chem. Int. Ed.* **2025**, *64*, e202415891.
127. Lee, J.; Nam, K.; Ku, B.; et al. 2D Phosphorene-Decorated Ni-Rich Layered Cathodes for High-Power and High-Energy Li-Ion Batteries. *Adv. Funct. Mater.* **2025**, e11385. https://doi.org/10.1002/adfm.202511385.
128. Yuan, K.; Tu, T.; Shen, C.; et al. Self-Ball Milling Strategy to Construct High-Entropy Oxide Coated $LiNi_{0.8}Co_{0.1}Mn_{0.1}O_2$ with Enhanced Electrochemical Performance. *J. Adv. Ceram.* **2022**, *11*, 882–892.
129. Zheng, J.; Xu, X.; Zhao, J.; et al. Design of Dual-Conducting Interface in Composite Cathode by semi-Cyclized Polyacrylonitrile Soft Coating for Practical Solid-State Lithium-Metal Batteries. *Energy Storage Mater.* **2025**, *74*, 103976.
130. Xu, Q.; Li, X.; Kheimeh Sari, H.M.; et al. Surface Engineering of $LiNi_{0.8}Co_{0.1}Mn_{0.1}O_2$ towards Boosting Lithium Storage: Bimetallic Oxides Versus Monometallic Oxides. *Nano Energy* **2020**, *77*, 105034.
131. Liang, J.; Zhu, Y.; Li, X.; et al. A Gradient Oxy-Thiophosphate-Coated Ni-Rich Layered Oxide Cathode for Stable All-Solid-State Li-Ion Batteries. *Nat. Commun.* **2023**, *14*, 146.
132. Li, Y.; Li, J.; Zeng, Z.; et al. Surface-Reconstructed High-Nickel Cathodes for Ultrastable 4.5 V Tolerant Sulfide-Based All-Solid-State Batteries. *ACS Energy Lett.* **2025**, *10*, 2203–2211.
133. Lin, Z.; Zhang, L.; Li, Y.; et al. In Situ Construction of an Electron-Withdrawing Polymer Coating Layer on NCM811 Interface for High-Performance Lithium-Ion Batteries. *Energy Storage Mater.* **2024**, *73*, 103876.
134. Ding, H.; Su, Y.; Wang, X.; et al. Enhancing the Cycling Stability of Nickel-Rich Oxide Cathode Materials through a Multifunctional CeO_2 Coating. *J. Colloid Interface Sci.* **2025**, *687*, 118–130.
135. Chu, Y.; Mu, Y.; Gu, H.; et al. Invoking Interfacial Engineering Boosts Structural Stability Empowering Exceptional Cyclability of Ni-Rich Cathode. *Adv. Mater.* **2024**, *36*, e2405628.
136. Wang, L.; Ding, G.; Yang, Z.; et al. Synergistic Construction of Uniform $LiAlO_2$ Coating on $LiNi_{0.8}Co_{0.1}Mn_{0.1}O_2$ Cathode Materials by Acid Etching and Polyvinylpyrrolidone Cross-Linking Approaches for High-Performance Li-Ion Batteries. *J. Alloys Compd.* **2024**, *990*, 174411.
137. Chen, Z.; Nguyen, H.D.; Zarrabeitia, M.; et al. Lithium Phosphonate Functionalized Polymer Coating for High-Energy $LiNi_{0.8}Co_{0.1}Mn_{0.1}O_2$ with Superior Performance at Ambient and Elevated Temperatures. *Adv. Funct. Mater.* **2021**, *31*, 2105343.
138. Xu, G.-L.; Liu, Q.; Lau, K.K.S.; et al. Building Ultra Conformal Protective Layers on both Secondary and Primary Particles of Layered Lithium Transition Metal Oxide Cathodes. *Nat. Energy* **2019**, *4*, 484–494.
139. Chu, Y.; Mu, Y.; Zou, L.; et al. Thermodynamically Stable Dual-Modified LiF&FeF_3 layer Empowering Ni-Rich Cathodes with Superior Cyclabilities. *Adv. Mater.* **2023**, *35*, e2212308.
140. Li, S.; Zhao, L.; Tan, J.; et al. Suppressing Stress-Induced Structural Degradation in $LiNi_{0.9}Co_{0.05}Mn_{0.05}O_2$ by High-Modulus Heterogeneous Coating. *Nano Energy* **2025**, *143*, 111294.
141. Luo, J.; Guo, B.; Li, N.; et al. Conductive Binary Li Borate Glass Coating for Improved Ni-Rich Positive Electrode in Sulfide-Based All-Solid-State Li Batteries. *Nat. Commun.* **2025**, *16*, 9462.
142. Ma, Y.; Teo, J.H.; Walther, F.; et al. Advanced Nanoparticle Coatings for Stabilizing Layered Ni-Rich Oxide Cathodes in Solid-State Batteries. *Adv. Funct. Mater.* **2022**, *32*, 2111829.
143. Liu, C.; Li, D.; Zhao, S.; et al. Atomic Layer Deposition of a Thin TiO_2 Layer on Nickel-Rich Cathode NCM83 for Improved Cycling Stability. *J. Mater. Chem. A Mater.* **2025**, *13*, 21748–21759.
144. Huang, K.; Xie, T.; Yang, H.; et al. Plasma-Assisted Sputter Li_3PO_4 Coating on NCM955 Cathodes Enhancing High-Temperature Cycling Performances. *J. Alloys Compd.* **2024**, *976*, 173232.
145. Wang, X.; Ren, D.; Liang, H.; et al. Ni Crossover Catalysis: Truth of Hydrogen Evolution in Ni-Rich Cathode-based Lithium-Ion Batteries. *Energy Environ. Sci.* **2023**, *16*, 1200–1209.
146. Huang, J.; Liu, J.; He, J.; et al. Optimizing Electrode/Electrolyte Interphases and Li-Ion Flux/Solvation for Lithium-Metal Batteries with Qua-Functional Heptafluorobutyric Anhydride. *Angew. Chem. Int. Ed.* **2021**, *60*, 20717–20722.
147. Yang, J.; Liu, X.; Wang, Y.; et al. Electrolytes Polymerization-Induced Cathode-Electrolyte-Interphase for High Voltage Lithium-Ion Batteries. *Adv. Energy Mater.* **2021**, *11*, 2101956.
148. Jiang, G.; Liu, J.; He, J.; et al. Hydrofluoric Acid-Removable Additive Optimizing Electrode Electrolyte Interphases with Li+ Conductive Moieties for 4.5 V Lithium Metal Batteries. *Adv. Funct. Mater.* **2023**, *33*, 2214422.
149. Jia, R.; Dai, H.; Tu, X.; et al. Hexabutylcyclohexane-1,2,3,4,5,6-hexaimine Additive-Assisted Commercial Ester Electrolyte for 4.7 V Highly-Stable Li-Metal Batteries. *Adv. Energy Mater.* **2023**, *13*, 2302747.
150. Kang, G.; Cao, Y.; Liu, Q.; et al. Efficient Screening of Electrolyte Additives for High-Temperature, High-Voltage Lithium Batteries via Fukui Functions. *Adv. Funct. Mater.* **2025**, e22713. https://doi.org/10.1002/adfm.202522713.
151. Kim, J.; Lee, D.G.; Lee, J.H.; et al. Concurrent Electrode-Electrolyte Interfaces Engineering via Nano-Si_3N_4 Additive for High-Rate, High-Voltage Lithium Metal Batteries. *Energy Environ. Sci.* **2025**, *18*, 3148–3159.

152. Sudoh, T.; Ikeda, S.; Shigenobu, K.; et al. Li-Ion Transport and Solution Structure in Sulfolane-Based Localized High-Concentration Electrolytes. *J. Phys. Chem. C* **2023**, *127*, 12295–12303.
153. Chen, S.; Zheng, J.; Mei, D.; et al. High-Voltage Lithium-Metal Batteries Enabled by Localized High-Concentration Electrolytes. *Adv. Mater.* **2018**, *30*, e1706102.
154. Ren, X.; Zou, L.; Cao, X.; et al. Enabling High-Voltage Lithium-Metal Batteries under Practical Conditions. *Joule* **2019**, *3*, 1662–1676.
155. Chen, S.; Zheng, J.; Yu, L.; et al. High-Efficiency Lithium Metal Batteries with Fire-Retardant Electrolytes. *Joule* **2018**, *2*, 1548–1558.
156. Lin, S.; Hua, H.; Lai, P.; et al. A Multifunctional Dual-Salt Localized High-Concentration Electrolyte for Fast Dynamic High-Voltage Lithium Battery in Wide Temperature Range. *Adv. Energy Mater.* **2021**, *11*, 2101775.
157. Zhang, B.H.; Chen, P.P.; Hou, Y.L.; et al. Localized High-Concentration Sulfone Electrolytes with High-Voltage Stability and Flame Retardancy for Ni-Rich Lithium Metal Batteries. *Small* **2024**, *20*, e2402123.
158. Chen, Y.; Zhao, Y.; Wang, A.; et al. Cosolvent Occupied Solvation Tuned Anti-Oxidation Therapy toward Highly Safe 4.7 V-Class NCM811 Batteries. *Energy Environ. Sci.* **2024**, *17*, 6113–6126.
159. Zhao, Y.; Zhou, T.; Baster, D.; et al. Targeted Functionalization of Cyclic Ether Solvents for Controlled Reactivity in High-Voltage Lithium Metal Batteries. *ACS Energy Lett.* **2023**, *8*, 3180–3187.
160. Weber, R.; Genovese, M.; Louli, A.J.; et al. Long Cycle Life and Dendrite-Free Lithium Morphology in Anode-Free Lithium Pouch Cells Enabled by a Dual-Salt Liquid Electrolyte. *Nat. Energy* **2019**, *4*, 683–689.
161. Zhong, S.; Dong, L.; Yuan, B.; et al. Stabilizing High-Nickel Cathodes via Interfacial Hydrogen Bonding Effects Using a Hydrofluoric Acid-Scavenging Separator. *Engineering* **2024**, *39*, 117–126.
162. Seo, J.-Y.; Lee, Y.-H.; Kim, J.-H.; et al. Electrode-Customized Separator Membranes Based on Self-Assembled Chiral Nematic Liquid Crystalline Cellulose Nanocrystals as a Natural Material Strategy for Sustainable Li-Metal Batteries. *Energy Storage Mater.* **2022**, *50*, 783–791.
163. Versaci, D.; Canale, I.; Goswami, S.; et al. Molybdenum Disulfide/Polyaniline Interlayer for LITHIUM Polysulphide Trapping in Lithium-Sulphur Batteries. *J. Power Sources* **2023**, *521*, 230945.
164. An, Q.; Liu, Q.; Mao, P.; et al. Developing the Tandem Structure to Regulate Interfacial Chemistry and Promote Ion Transport Kinetics Toward High-Voltage Lithium Metal Batteries. *Angew. Chem. Int. Ed.* **2025**, *64*, e202422539.
165. Wang, Y.; Ji, M.; Zhu, T.; et al. Multifunctional Amino-Functionalized Zr-Based Metal-Organic Frameworks: A Breakthrough in Enhancing the Stability and Performance of Ni-Rich Cathode Li Metal Batteries in Water-Prone Environments. *Energy Storage Mater.* **2025**, *77*, 104217.
166. Zeng, H.; Wang, Q.; Liu, C.; et al. Dynamics-Enhanced Sandwich Solid-State Electrolyte Separator for Wide-Temperature Operation of Lithium Metal Batteries. *Energy Storage Mater.* **2025**, *82*, 104614.
167. Han, D.-Y.; Lee, J.; Bang, Y.; et al. Molecularly Engineered Membrane-Driven Interphase Stabilization of Electrodes for Li||NCM811 Cells Under Practical Operating Conditions. *Energy Environ. Sci.* **2025**, *18*, 10112–10124.
168. Liao, C.; Zheng, T.; Zhu, J.; et al. Engineering Durable Nitrate-Enriched Solvation Sheaths in Carbonate Electrolytes through Functional Separator Design for High-Voltage Lithium Metal Batteries. *Nano Energy* **2025**, *142*, 111283.
169. Zhu, H.; Zhang, G.; Song, M.; et al. Coordination-Induced High-Dielectric Polymer Coatings for High-Energy-Density Lithium Batteries. *Energy Storage Mater.* **2023**, *63*, 102968.
170. Li, X.; Liu, K.; Yan, Y.; et al. Thermostable and Nonflammable Polyimide/Zirconia Compound Separator for Lithium-Ion Batteries with Superior Electrochemical and Safe Properties. *J. Colloid Interface Sci.* **2022**, *625*, 936–945.
171. Wu, D.; Dong, N.; Wang, R.; et al. In Situ Construction of High-Safety and Non-Flammable Polyimide “Ceramic” Lithium-Ion Battery Separator via SiO_2 Nano-Encapsulation. *Chem. Eng. J.* **2021**, *420*, 129992.
172. Chen, X.; Liu, J.; Li, W.; et al. Permselective Covalent Organic Framework Membrane as Self-Extinguishing Separator for High-Safety Lithium-Ion Battery. *Angew. Chem. Int. Ed.* **2025**, *64*, e202512591.
173. Niu, C.; Luo, W.; Dai, C.; et al. High-Voltage-Tolerant Covalent Organic Framework Electrolyte with Holistically Oriented Channels for Solid-State Lithium Metal Batteries with Nickel-Rich Cathodes. *Angew. Chem. Int. Ed.* **2021**, *60*, 24915–24923.
174. An, H.; Li, M.; Liu, Q.; et al. Strong Lewis-Acid Coordinated PEO Electrolyte Achieves 4.8 V-Class All-Solid-State Batteries over 580 $Wh \cdot kg^{-1}$. *Nat. Commun.* **2024**, *15*, 9150.
175. Hou, J.; Sun, W.; Yuan, Q.; et al. Multiscale Engineered Bionic Solid-State Electrolytes Breaking the Stiffness-Damping Trade-Off. *Angew. Chem. Int. Ed.* **2025**, *64*, e202421427.
176. Eckert, H.; Rodrigues, M.-A. Ion-Conducting Glass-Ceramics for Energy-Storage Applications. *MRS Bull.* **2017**, *42*, 206–212.